LJMU Research Online

Onori, F, Nicholl, M, Ramsden, P, McGee, S, Roy, R, Li, W, Arcavi, I, Anderson, JP, Brocato, E, Bronikowski, M, Cenko, SB, Chambers, K, Chen, TW, Clark, P, Concepcion, E, Farah, J, Flammini, D, González-Gaitán, S, Gromadzki, M, Gutiérrez, CP, Hammerstein, E, Hinds, KR, Inserra, C, Kankare, E, Kumar, A, Makrygianni, L, Mattila, S, Matilainen, KK, Müller-Bravo, TE, Petrushevska, T, Pignata, G, Piranomonte, S, Reynolds, TM, Stein, R, Wang, Y, Wevers, T, Yao, Y and Young, DR

 The case of AT2022wtn: a tidal disruption event in an interacting galaxy

https://researchonline.ljmu.ac.uk/id/eprint/26396/

Article

For more information please contact

The case of AT2022wtn: a tidal disruption event in an interacting galaxy

F. Onori [1]★ M. Nicholl [2] P. Ramsden,[2,3] S. McGee,[3] R. Roy [4] W. Li,[5] I. Arcavi,[5] J. P. Anderson,[6,7] E. Brocato [1,8] M. Bronikowski,[9] S. B. Cenko,[10,11] K. Chambers,[12] T. W. Chen,[13] P. Clark,[14] E. Concepcion,[9] J. Farah,[15,16] D. Flammini,[17] S. González-Gaitán [6,18] M. Gromadzki [19] C. P. Gutiérrez [20,21] E. Hammerstein,[10,22,23] K. R. Hinds [24] C. Inserra [25] E. Kankare,[26] A. Kumar [27] L. Makrygianni,[28] S. Mattila,[26,29] K. K. Matilainen,[26] T. E. Müller-Bravo,[20,21] T. Petrushevska,[9] G. Pignata,[30] S. Piranomonte,[8] T. M. Reynolds [26,31,32] R. Stein,[33] Y. Wang [34] T. Wevers [35,36] Y. Yao[37,38] and D. R. Young[2]

Affiliations are listed at the end of the paper

ABSTRACT

We present the results from our multiwavelength monitoring campaign of the transient AT 2022wtn, discovered by the Zwicky Transient Facility in the nucleus of SDSS J232323.79 + 104107.7, the less-massive galaxy in an active merging pair with a mass ratio of $\sim$10:1. AT 2022wtn shows spectroscopic and photometric properties consistent with a X-ray faint N-strong TDE-H + He with a number of peculiarities. Specifically, a 30-d long plateau at maximum luminosity, a corresponding dip in temperature and the development of a double-horned N III + He II line profile. Strong and time-evolving velocity offsets in the tidal disruption event (TDE) broad emission lines and the detection of a transient radio emission, indicate the presence of outflows. Overall, the observed properties are consistent with the full disruption of a low-mass star by a $\sim 10^6 \, M_\odot$ supermassive black hole followed by an efficient disc formation and the launch of a quasi-spherical reprocessing envelope of fast expanding outflowing material. The observed differences between the He II and the Hydrogen and N III lines can be explained either with a spatial separation of the lines emitting region or with a late-time reveal of shocks from the returning debris streams, as the photosphere recedes. Finally, we present an extensive analysis of the hosting environment and discuss the implications for the discovery of two TDEs in interacting galaxy pairs, finding indication for an over-representation of TDEs in these systems. The AT 2022wtn host galaxy properties suggest that it is in the early stages of the merger, therefore we may be witnessing the initial enhanced rate of TDEs in interacting galaxies before the post-starburst phase.

Key words: black hole physics – galaxies: individual: AT2022wtn; SDSSJ232323.79 + 104107.7 – galaxies: interactions – galaxies: nuclei – transients: tidal disruption events.

1 INTRODUCTION

When a star approaches a supermassive black hole (SMBH), it can be ripped apart by the strong tidal forces at play if they overcome the star's self-gravity. This results in a tidal disruption event (TDE, Rees 1988; Evans & Kochanek 1989; Phinney 1989). During these phenomena, approximately half of the stellar material is expelled in unbound orbits, while the rest streams back to the SMBH, it is stretched into elongated streams, and it starts a circularization process into highly eccentric orbits, which ends with the formation of a new accretion disc around the involved SMBH. The peak of the TDE emission is in the X-rays and/or ultraviolet (UV)/optical bands, and in some cases it can even exceed the Eddington luminosity of the SMBH (Strubbe & Quataert 2009; Lodato & Rossi 2011; Wevers et al. 2019b). Observationally, TDEs give rise to a short-lived and luminous ($L_{\rm bol} \sim 10^{41-45}$ erg s^{-1}) transient flare located in

the nuclear regions of the hosting galaxy. These galaxies are typically quiescent, with an observed overabundance of TDEs detected in post-starburst/E + A host galaxies (Arcavi et al. 2014; French, Arcavi & Zabludoff 2016; Graur et al. 2018; French et al. 2020). Interestingly, a recent work of Wevers & French (2024) has shown that TDEs are strongly over-represented in gas-rich post-starburst galaxies with faded active galactic nuclei (AGNs) and extended emission-line regions, indicating that they may have had a merger very recently.

These phenomena are particularly interesting for a number of reasons. They represent an extraordinary laboratory for studying black holes (BHs, i.e. they are used to directly constrain the mass and spin of BHs) and accretion-related phenomena on human-friendly time-scales. Given that the star's disruption can only occur outside the BH horizon event, they are an excellent tool to unveil dormant SMBHs in the low-mass end of the SMBH mass distribution ($M_{\rm BH} \leq 10^7 \, M_\odot$, above $\sim 10^8 \, M_\odot$ the star is swallowed whole), including the elusive population of intermediate-mass BHs. The occurrence of TDEs can be used to probe the SMBH occupation fraction in different types of galaxies (Metzger & Stone 2016), and their rate and

★ E-mail: francesca.onori@inaf.it

their evolution over time can provide important information on the existence of SMBHs at high redshift (Mortlock et al. 2011). Finally, TDEs are multimessenger phenomena, being candidate sources of high-energy neutrinos (Stein et al. 2021; Reusch et al. 2022), and gravitational wave (GW) sources potentially detectable by future space-based interferometers (Toscani, Rossi & Lodato 2020; Ajith et al. 2025, but see also the work of Wevers & Ryu 2023, for different results on the TDEs GW detectability).

TDEs were predicted to be brightest in X-rays, and indeed the first candidates were discovered as luminous X-ray transient sources in the *ROSAT* all sky survey archive (Komossa & Bade 1999) and, subsequently, other TDEs were revealed through dedicated searches or serendipitous discoveries with the *Chandra*, *XMM–Newton*, and *Swift* satellites (Esquej et al. 2007, 2008; Saxton et al. 2012; Komossa 2015; Saxton et al. 2020). However, in the last decade, thanks to the availability of increasingly efficient wide-field optical surveys, specifically designed to search for transient phenomena, the sample of TDEs has rapidly grown from a few candidates to tens of confirmed TDEs and the optical band has become their primary discovery channel. A population of transients with some well-established key observational features has been revealed, but also characterized by a broad range of properties, with each event still providing new clues but raising new questions (see the reviews from van Velzen et al. 2020; Gezari 2021). Indeed, recent researches found a few nuclear transients with ambiguous properties, which were initially classified as TDEs (cf. Neustadt et al. 2020; Hinkle et al. 2022; Roy et al. 2024, and references therein).

The UV/optical light curves are characterized by persistent blue colours (i.e. $g - r < 0$), relatively long time-scales for the rise to the peak luminosity (<30 d) if compared to most typical supernovae (SNe), and a smooth, power-law decline broadly consistent with $L \propto t^{-5/3}$ law (following the predicted fall-back rate on to the BH), which can last from months to years (although recently a great diversity in light-curve shapes has been revealed, van Velzen et al. 2011, 2020). The blackbody (BB) temperatures are usually high ($T_{BB} \sim 10^4$ K) and approximately constant over the whole transient evolution, but they are also accompanied by a time-evolving BB radius (van Velzen et al. 2021). In the early phases, the optical spectra are typically dominated by a strong, hot, and blue thermal continuum and by very broad ($\sim 10^4$ km s^{-1}) H and/or He lines characterized by a pure emission profile and with different relative ratios (Arcavi et al. 2014; Leloudas et al. 2019; Charalampopoulos et al. 2022). In some cases, broad Bowen fluorescence emission lines and evidence for the presence of Fe II multiplets have been identified (Blagorodnova et al. 2019; Leloudas et al. 2019; Onori et al. 2019; Wevers et al. 2019b; Cannizzaro et al. 2021). This spectral variety led to the division of the TDE population into three main spectral classes, on the basis of the presence or lack of the main broad emission lines: the TDE-H, TDE-H + He (most of them showing also Bowen features), and TDE-He (Arcavi et al. 2014; van Velzen et al. 2020, 2021). However, this classification may be time dependent, as evidenced by some TDEs with spectral lines that appear or disappear in time (e.g. AT2017eqx and AT 2017gge: Nicholl et al. 2019; Onori et al. 2022). The interaction of the TDE flare with the host galaxy's environment can result in reverberation signals (IR echoes and transient long-lasting high ionization coronal emission lines, Lu, Kumar & Evans 2016; van Velzen et al. 2016; Jiang et al. 2021; Onori et al. 2022; Short et al. 2023), which trace the circumnuclear hosting environment and can be used as additional discovery channels. Indeed, recently, a number of TDEs have been identified also thanks to the observation of transient mid-infrared flares (Mattila et al. 2018; Kool et al. 2020; Jiang et al. 2021; Reynolds et al. 2022; Masterson et al. 2024).

Thanks to the growth of the TDE sample together with the increasing use of a multiwavelength approach in the observing strategies, a crucial dichotomy in the TDE population has been revealed. Specifically, among the optically selected TDEs, only few events show X-rays at the time of the optical peak, and instead a delayed X-ray emission was detected in some notable cases (e.g ASASSN-14li, ASASSN-15oi, AT 2019dsg, AT 2018fyk, AT 2019qiz, AT 2019azh, AT 2017gge; Holoien et al. 2016b; Gezari, Cenko & Arcavi 2017; Wevers et al. 2019a; Nicholl et al. 2020; Cannizzaro et al. 2021; Liu et al. 2022; Onori et al. 2022, respectively). Interestingly, from recent studies it has emerged that a large fraction of optical-selected X-rays faint TDEs (>40 per cent) do show X-rays emission at later times (Jonker et al. 2020; Guolo et al. 2024). These discoveries have led to questions about both the origin of the TDE prompt emission mechanism and the properties of the emission region itself and different theoretical scenarios have been thus proposed, which are still under debate. The strong UV/optical emission is ascribed either to the occurrence of shocks between self-intersecting debris streams well before the end of the circularization process and the formation of the accretion disc (Piran et al. 2015; Shiokawa et al. 2015; Jiang, Guillochon & Loeb 2016; Steinberg & Stone 2024), or to reprocessing of the X-rays emitted by a newly formed accretion disc (Guillochon & Ramirez-Ruiz 2013; Guillochon, Manukian & Ramirez-Ruiz 2014; Metzger & Stone 2016; Roth et al. 2016). The latter scenario needs the presence of an optically thick reprocessing layer which can arise either as a consequence of super-Eddington accretion induced outflows (Miller et al. 2015; Thomsen et al. 2022) or collision-induced outflows at the streams self-intersection point (Lu & Bonnerot 2020; Bonnerot, Lu & Hopkins 2021) or a promptly and rapidly circularization of the debris stream which cools inefficiently (cooling envelope model, Metzger 2022). In the TDE unified model of Dai et al. (2018), optically thick winds produced following the formation of the accretion disc are responsible for the X-ray obscuration and viewing angle effects together with the intrinsic physical properties of the electromagnetic emitting region determine the detection of the X-ray emission.

1.1 AT 2022wtn: the discovery

The discovery of AT 2022wtn was first announced by the Zwicky Transient Facility (ZTF, Bellm et al. 2019) on 2022 October 2 (MJD 59 854.26), which reported the observation of a new optical transient at magnitude $g' = 19.57$ mag, internally labelled as ZTF22abkfhua. The transient is located at coordinates RA (J2000) = 23:23:23.772, Dec. (J2000) = +10:41:07.83, consistent with the nucleus of the galaxy SDSS J232323.79+104107.7. This galaxy is undergoing a merger with the more massive galaxy SDSS J232323.37 + 104101.7, as shown in the Legacy Survey DR10 image of the AT 2022wtn field (see Fig. 1). Thanks to spectroscopic observations on 2022 November 21, the nuclear transient was identified as a TDE at $z = 0.049$ (TNS Classification Report No. 13873, Fulton et al. 2022).

AT 2022wtn was observed with NSF's Karl G. Jansky Very Large Array (VLA) on 2023 January 8 and 2023 March 21 (MJD 59 952 and MJD 60 024, respectively) at a mean frequency of 15 GHz and the detection of an emission coincident with the AT 2022wtn position was reported by Christy et al. (2023) (ATel no. 15972). In particular, while in the first epoch the detection was only marginal, the source clearly brightened in the second observation, rising from a flux density of $20 \pm 7 \mu$Jy to a flux density of $223 \pm 6 \mu$Jy and, thus, confirming the transient nature of the detected radio emission.

We here report the result from the UV/optical and X-ray follow-up campaign covering a total of ~ 393 d from the transient discovery.
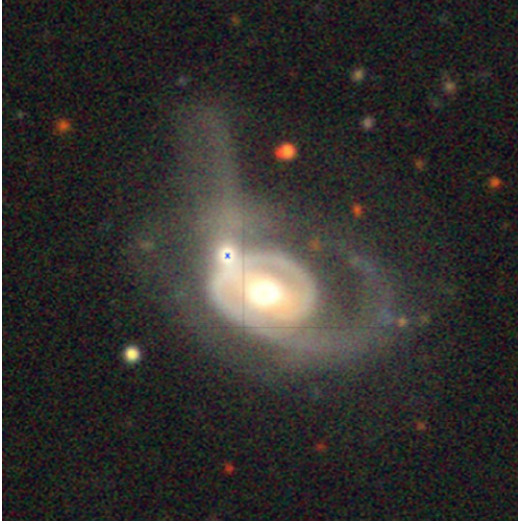
Figure 1. Legacy Survey DR10 image of the AT 2022wtn field. The TDE occurred on the nucleus of the smaller interacting galaxy as indicated by the blue cross. The tidal tails resulting from the merging interaction between the two galaxies are well visible.

Throughout the paper, all the phases are referenced with respect to the transient's discovery date (unless otherwise specified) and a luminosity distance of $d_L = 219.9$ Mpc, based on a *WMAP*9 (*Wilkinson Microwave Anisotropy Probe*) cosmology with $H_0 = 69.32$ km s^{-1} Mpc^{-1}, $\Omega_M = 0.29$, and $\Omega_\Lambda = 0.71$ (Hinshaw et al. 2013) is used.

2 OBSERVATIONS AND DATA REDUCTION

In order to provide a good coverage and characterization of the AT 2022wtn emission, we promptly started a long-lasting monitoring campaign, characterized by a multiwavelength approach and including photometric and spectroscopic observations. In the following, we describe the observational set-up and the data reduction for each instrument used.

2.1 Optical photometry

In Fig. 2, the AT2022wtn UV/optical light curve is shown for a total of 250 d. The rise and the peak phases (corresponding to the first $\sim$ 100 d) are densely monitored by the ZTF, the Asteroid Terrestrial-impact Last Alert System (ATLAS, Smith et al. 2020), and and the Panoramic Survey Telescope and Rapid Response System (Pan-STARRS, Huber et al. 2015; Chambers et al. 2016) transient surveys, which delivered host-subtracted magnitudes measurements in the g', r', c, and o filters, respectively. ZTF data have been retrieved from Lasair alert stream broker (Smith et al. 2019); calibrated ATLAS data in the cyan (c) and orange (o) bands were obtained using the ATLAS forced photometry service (Tonry et al. 2018; Smith et al. 2020; Shingles et al. 2021). We rebinned the four exposures obtained on each night into a single nightly measurement to improve the signal-to-noise ratio. Pan-STARRS host-subtracted magnitudes in the w band are also available during the first $\sim$50 d of the transient evolution. Pan-STARRS (PS) observations are processed and photometrically calibrated with the PS image processing pipeline (Waters et al. 2020; Magnier et al. 2020a, b).

We obtained additional images in the u', g', r', and i' filters with the Optical Wide Field Camera (IO:O), mounted on the 2.0-m Liverpool Telescope (LT, Steele et al. 2004) located at the Roques de los
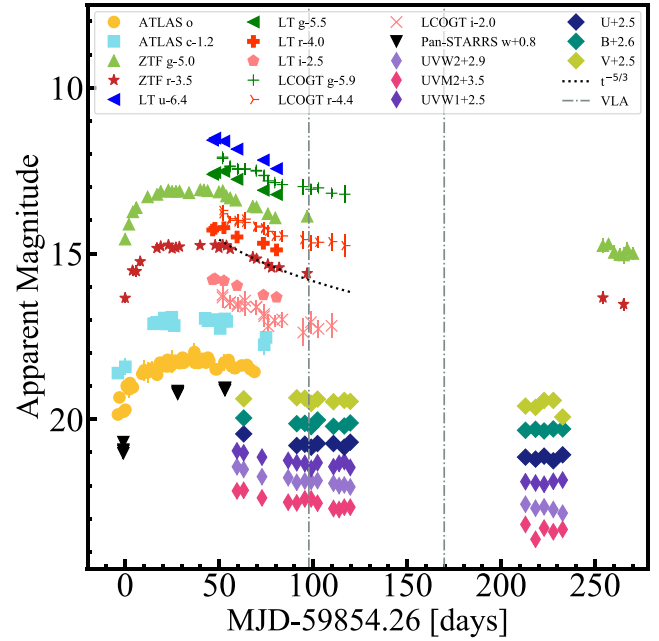

Figure 2. AT 2022wtn UV/optical light curve. The optical data are host-subtracted. Magnitudes are reported in the AB system and are not corrected for foreground extinction. Vertical dot–dashed grey lines show the location of the VLA detection. We show the $t^{-5/3}$ decline with a dotted line overplotted on the ZTF r' points.

Muchachos Observatory in La Palma island (Spain), and with the Las Cumbres Observatory (LCOGT,[1] Brown et al. 2013) global network of 1.0-m telescopes. These observations cover the post-peak phase between $\sim$50 and $\sim$100 d from the transient discovery. We processed the IO:O/LT images by using the instrument pipeline,[2] while the photometry was derived by using a custom pipeline, Photometry Sans Frustration[3] (Nicholl et al. 2023), which is a PYTHON-based code employing both aperture and point-spread-function (PSF) fitting photometry routines from ASTROPY and PHOTUTILS. The g', r', and i' zero-points were derived by using reference stars from Pan-STARRS, while for the u' we used SDSS stars. Image subtraction was performed by using PYZOGY (Zackay, Ofek & Gal-Yam 2016; Guevel & Hosseinzadeh 2017) and pre-transient templates images from Pan-STARRS (g', r', and i') and SDSS (u'). Finally, the photometry measurements were performed by fitting the PSF on each host-subtracted images.

Also in the case of the optical imaging data from LCOGT, the suppression of the host-galaxy contamination have been performed by using the PYZOGY package, while the photometric measurements have been performed by applying PSF photometry with the AUTOmated Photometry Of Transients pipeline (AUTOPHOT, Brennan & Fraser 2022). In Table B1, we list the photometric measurements derived for the host-subtracted I:IO and LCOGT data. The apparent magnitudes are reported in the AB system and not corrected for foreground extinction. Instead, archival photometry available for both for the AT 2022wtn host and the neighbouring galaxy is reported in Table 1.

Table 1. Archival photometry of the AT 2022wtn host and for the interacting galaxy, SDSS J232323.37 + 104101.7, taken from SDSS DR16 (u', g', r', i', and z', in AB system), and from 2MASS (J, H, and K_s) catalogues.

Filters (mag)	SDSS J232323.79 + 104107.7 (AT 2022wtn host)	SDSS J232323.37 + 104101.7
u'	18.987 ± 0.084	17.75 ± 0.02
g'	17.305 ± 0.008	16.03 ± 0.00
r'	16.692 ± 0.007	15.21 ± 0.00
i'	16.301 ± 0.008	14.75 ± 0.00
z'	16.062 ± 0.019	14.42 ± 0.00
J	15.950 ± 0.150	14.125 ± 0.052
H	15.451 ± 0.221	13.363 ± 0.063
K_S	14.790 ± 0.192	12.932 ± 0.057

2.2 UVOT photometry and X-ray non-detection

We accurately monitor the UV and X-ray emission with the UltraViolet and Optical Telescope (UVOT) and the X-Ray Telescope (XRT) instruments on board of the Neil Gehrels *Swift* observatory (Gehrels et al. 2004) following the transient peak. Specifically, a total of 17 *Swift*/UVOT + XRT observations have ensured the monitoring of the UV/optical and X-rays emission between ∼60 and ∼230 d from the transient discovery (see Table B2 for the log of the observations).

The *Swift*/UVOT observations include images in the filters *UVW*2 (1928 Å), *UVM*2 (2244 Å), *UVW*1 (2600 Å), *U* (3465 Å), *B* (4392 Å), and *V* (5468 Å) which have been reduced using the standard pipeline with the updated calibrations from the HEASOFT-6.28 FTOOLS package. In order to derive the apparent magnitudes of the transient we used the HEASOFT routine `uvotsource`. For each filter, we measured the aperture photometry using a 5 arcsec aperture centred on the position of the transient and a background region of 60 arcsec radius placed in an area free of sources. In Table B2, we show the values obtained from the *Swift*/UVOT photometric measurements for all the filters. The apparent magnitudes are reported in the Vega system and uncorrected for foreground extinction. In the last row of Table B2, we also report the host contribution in the UVOT filters as derived from the host galaxy spectral energy distribution (SED) fitting, described in more detail in Section 5.1. We used these synthetic host photometric values to subtract the host galaxy contribution in all the UVOT filters, but the *B* and *V* bands, where the galaxy is much brighter. For these two cases, we measured the host galaxy flux using the last UVOT epoch (MJD 60 087), when the host galaxy dominates the transient contribution.

Along with the UVOT, the *Swift* onboard XRT telescope also observed the transient in the energy range 0.3−10 keV. However, nothing was detected in XRT, even after stacking all of the X-ray images of the field (count rate $< 1.89 \times 10^{-3}$ counts s^{-1}). The X-ray non-detection of AT2022wtn along with the detection of some of the probable Bowen fluorescence lines may have significant implications in understanding the nature of the transient (see Section 4.1.1).

2.3 Optical spectroscopy

Our spectroscopic follow-up started ∼5 d after the transient discovery and it has been carried out by using the following facilities: the SEDm achine (SEDM, Blagorodnova et al. 2018) mounted on the Palomar 60-inch telescope (P60), located at the Palomar Observatory (USA), the SPectrograph for the Rapid Acquisition of Transients (SPRAT, Piascik et al. 2014) mounted on the LT, the Folded Low Order whYte-pupil Double-dispersed Spectrograph (FLOYDS) spectrograph installed on the LCOGT 2m telescope Faulkes Tele-

scope North (FTN) located at the Haleakala observatory (Hawaii), the DeVeny Spectrograph mounted at the 4.3-m Lowell Discovery Telescope (LDT) located in Flagstaff (Arizona), the ESO Faint Object Spectrograph and Camera (EFOSC2, Buzzoni et al. 1984), mounted on the 3.58-m New Technology Telescope (NTT), and the Low Resolution Imaging Spectrometer (LRIS, Oke et al. 1995) operating at the Cassegrain focus of the 10-m Keck I telescope, located at the W. M. Keck Observatory in Maunakea island (Hawaii). Two spectra of the neighbour galaxy SDSS J232323.37 + 104101.7 have been also taken with the the DeVeny and the EFOSC2 spectrographs.

All the spectra were reduced in a standard manner which include bias, flat-field, cosmic ray correction and wavelength, and flux calibration via arc lamp and standard star spectra. In Table 2, the list of the spectroscopic observation and their main properties, such as the date of the observation, the instrument used, the exposure times, the airmass, and seeing, is reported. The sequence of the optical spectra is shown in Fig. A1.

2.4 The spectroscopic instrumentation

In the following, we describe the details of the spectroscopic instrumentation used:

(i) The first spectrum of AT 2022wtn was taken 4.98 d after the transient discovery with SEDM. This is a very low resolution spectrograph operating at $R = \lambda/\Delta\lambda \sim 100$ in the 4000–8000 Å wavelength range. Data are reduced by using the SEDM automatic pipeline.[4]

(ii) We obtain two AT 2022wtn spectra with SPRAT at 23.66 and 49.58 d from the transient discovery. This low resolution ($R \sim 350$, for a 1.8 arcsec slit width) spectrograph, operates in the 4020–8100 Å wavelength range. Data are reduced by using an adaption of the `frodospec`[5] automatic pipeline.

(iii) Two additional spectra at 53.20 and 62.17 d were observed with the FLOYDS spectrograph on the FTN of the LCOGT network. These spectra cover 3500–10 000 Å, at a resolution $R \approx 400 - 700$ (at the blue and red end, respectively) and were taken at the paralactic angle. The spectra were reduced using the `floydsspec` pipeline[6] and the final spectrum extraction is described in Valenti et al. (2014).

(iv) The DeVeny spectrograph works in a broad wavelength range, between 3200 Å and 1 μm, with a moderate resolution ranging between $R = 500$ and 4000, depending upon the grating used. We obtain one AT 2022wtn spectrum at 59.91 d and one spectrum of the neighbour interacting galaxy SDSS J232323.37 + 104101.7 during the same night. We used the grating DV2 which covers the 3000–7400 Å wavelength range with a dispersion of 2.17 Å pixel^{-1} and R = 920. Data have been reduced by using the PYTHON-based pipeline `PypeIt`.[7]

(v) We have obtained a total of three AT 2022wtn spectra and one spectrum of the neighbour galaxy (SDSS J232323.37+104101.7) with the EFOSC2 instrument in the framework of the advanced ePESSTO + ESO public spectroscopic survey (Smartt et al. 2015). In all the cases, we used the grism Gr no. 13, which covers the 3650–9250 Å wavelength range and provides a resolution of $R = \lambda/\Delta\lambda \sim$ 300 for a 1.0 arcsec slit (a slightly higher resolution is achieved for seeing better than 1.0 arcsec). We used a slit width of 1.0 or 1.5 arcsec, depending on the seeing condition during the observations, oriented

[4] https://github.com/MickaelRigault/pysedm
[5] https://telescope.livjm.ac.uk/TelInst/Pipelines/#frodospecL2
[6] https://github.com/svalenti/FLOYDS_pipeline/
[7] https://pypeit.readthedocs.io/en/latest/

Table 2. List of spectroscopic observation of AT 2022wtn.

MJD (d) (1)	Phase (d) (2)	Instrument (3)	R ($\lambda/\Delta\lambda$) (4)	Exp. time (s) (5)	Airmass (arcsec) (6)	Seeing (arcsec) (7)
59 859.24	4.98	SEDM	100	2250	1.086	
59 877.91	23.66	SPRAT-B	350	600	1.056	2.256
59 903.84	49.58	SPRAT-B	350	2100	1.057	1.068
59 907.46	53.20	FLOYDS	400–700	3600	1.711	2.785
59 914.18	59.91	DeVeny	920	900	1.25	1.00
59 914.18*	59.91	DeVeny	920	900	1.25	1.00
59 916.43	62.17	FLOYDS	400–700	3600	1.639	2.729
59 934.04	79.78	EFOSC2-Gr no. 13	300	2700	1.778	0.970
59 960.22	105.96	KECK-LRIS	600/1000	600	1.532	
60 086.39	232.13	EFOSC2-Gr no. 13	300	2×1800	1.581	2.30
60 086.39*	232.13	EFOSC2-Gr no. 13	300	2×1800	1.581	2.30
60 247.10	392.84	EFOSC2-Gr no. 13	300	2×1800	1.330	1.10

Notes. (1) Date of observation; (2) days after discovery; (3) instrument used; (4) spectral resolution; (5) exposure time; (6) airmass; and (7) seeing.
* Spectrum of the neighbour galaxy SDSS J232323.37 + 104101.7.

at the parallactic angle. All the spectra have been reduced by using the ePESSTO NTT Pipeline v.2.4.0,[8] which is based on standard IRAF tasks. Multiple spectra taken on the same night are averaged in order to increase the Signal to Noise Ratio (S/R).

(vi) One spectrum was taken with LRIS 105.96 d. This instrument is characterized by a broad wavelength coverage (3200–10 000 Å), obtained thank to the simultaneous observation of two arms (operating in the red and in the blue part of the spectrum, respectively). A variety of available gratings (red side) and grisms (blue side) yield resolutions ranging from $R = 300$ and 5000. Our observations were carried out in long-slit mode, with a slit width of 1.0 arcsec oriented at the parallactic angle. We used the the grism 400/3400 for the blue camera, yielding an $R \sim 600$ (calculated for a 1.0 arcsec slit width) and the grating 400/8500 for the red camera, which yields to a resolution of $R\sim1000$ (for a 1.0 arcsec slit width). Data are reduced with the instrument dedicated software package LPIPE (Perley 2019).

3 PHOTOMETRIC ANALYSIS

In Fig. 2, we show the AT 2022wtn optical/UV light curve, with magnitude offsets applied to each filter for clarity. All the optical magnitudes are host-subtracted, but not yet corrected for foreground extinction. Already at this initial stage of the analysis, the overall light-curve behaviour is clear. It is characterized by a peak value of $r' = 18.34 \pm 0.05$ mag, reached after a rising phase of ~20 d. Remarkably, it remains around this value for ~30 d before starting the declining phase.

In order to investigate on the physical properties of the UV/optical emission, we computed the bolometric luminosity by using the AT 2022wtn host-subtracted multicolour photometry as input values in the PYTHON-based routine superbol (Nicholl 2018). All the used magnitudes are corrected for the Galactic extinction from Schlafly & Finkbeiner (2011) assuming a reddening law with $R_V = 3.1$ and $A_v = 0.2073$ (mag), and K-correction (Oke & Sandage 1968) has been also applied. When needed, we derived the missing magnitudes values by extrapolating the photometry assuming a constant colour evolution for the light curve. We calculated the pseudo-bolometric luminosity by integrating over the observed fluxes and by fitting with a single BB function the SED inferred from the multicolour data
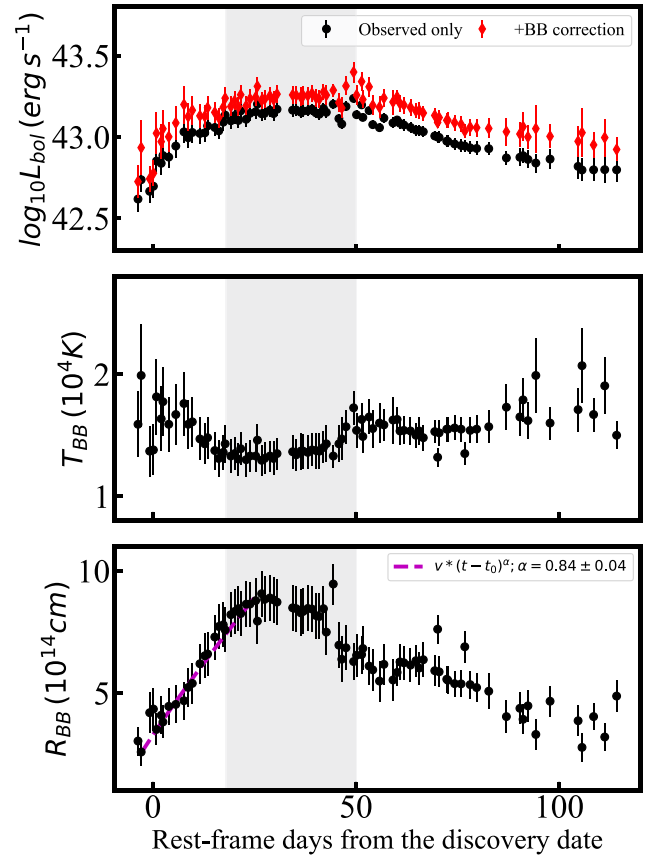
[8]https://github.com/svalenti/pessto

Figure 3. Superbol output showing the pseudo-bolometric light curve (upper panel), the T_{BB} (central panel), and the R_{BB} (bottom panel) time evolution. The input magnitudes are host-subtracted and have been corrected for reddening. The data are plotted with a bin of 1 d. Grey area indicate the duration of the maximum luminosity plateau phase. The magenta dashed line in the bottom panel shows the best fit for the R_{BB} rising phase.

for each epoch. We used the best-fitted BB model to compute the additional flux bluewards of the *UVW*2 band and redwards of *i* band.

The results are shown for the first 100 d of the transient evolution in Fig. 3. In the upper panel, the pseudo-bolometric luminosity derived by using the two different methods is shown. The BB temperature and
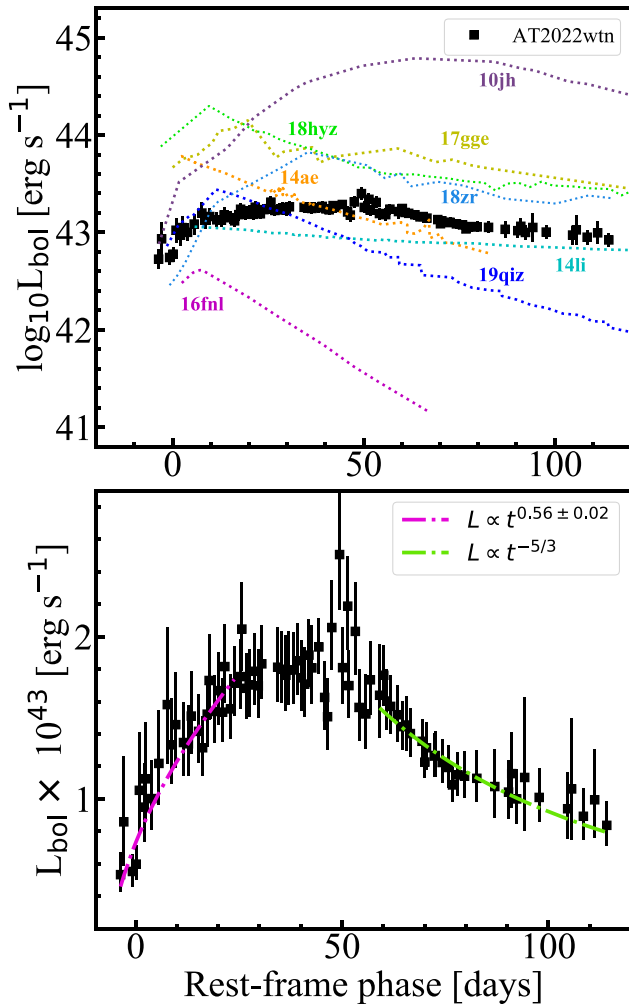
Figure 4. Upper panel: pseudo-bolometric luminosity of AT2022wtn in comparison with other TDE light curves. Lower panel: results from the fit of the rising (magenta dash–dotted line) and declining (green dash–dotted line) phase of the AT 2022wtn pseudo-bolometric luminosity.

radius evolution with time are shown in the centre and bottom panels, respectively. The same time evolution exhibited by the optical/UV light curve is clearly visible also in the pseudo-bolometric luminosity. Specifically, after an initial rising phase, it reaches a maximum luminosity plateau, lasting about 30 d, during which the luminosity has an averaged value of $<\log(L_{\rm BB,max})> = 43.13 \pm 0.06$ erg s^{-1}. By using the PYTHON tool CURVEFIT, we modelled the rise of the pseudo-bolometric luminosity with a power law of the form $L_{\rm BB} = L_{\rm (BB,0)} ((t-t_0)/\tau)^a$ and we obtain an initial time $t_0 = -6.6 \pm -2.6$ d, a rising time-scale $\tau = 11.5 \pm 3.4$ d, and a power-law index $a = 0.56 \pm 0.14$. Moreover, we also model the first 50 d of the decline of the light curve with the power law $L_{\rm BB} \propto ((t-t_0)/\tau)^{-5/3}$, by fixing $t_0 = -6.6 \pm -2.6$ d (i.e. the value obtained from the fit of the rising phase). The results are shown in the bottom panel of Fig. 4.

A comparison with the pseudo-bolometric light curves of a compilation of TDEs, computed by applying the same method used for AT 2022wtn is shown in the upper panel of Fig. 4. In particular, the photometric data of iPTF16fnl and of AT 2017gge are taken from Onori et al. (2019, 2022), respectively, while, for the other TDEs we retrieve the data from Gezari et al. (2012), Holoien et al. (2014, 2016a), van Velzen et al. (2019), Gomez et al. (2020), and Nicholl et al. (2020), respectively. AT 2022wtn is placed in the middle of the

others TDEs light curves, with the luminosity consistent with the values usually expected for these transients.

As expected in the case of a TDE, the BB temperature is consistent with being constant at a value of $T_{\rm BB} \sim 1.55 \times 10^4$ K, although, between $\sim$20 and $\sim$40 d from the transient discovery (consistent with the luminosity maximum plateau phase), it constantly remains at a slightly lower value ($T_{\rm BB} \sim 1.35 \times 10^4$ K). Instead, there is a clear evolution of the BB radius with time, starting from initial values of about $R_{\rm BB} \sim 3 \times 10^{14}$ cm and rising over the first 25 d of the transient evolution to a maximum value of about $R_{\rm BB} \sim 9 \times 10^{14}$ cm. The BB radius remains around this value for a total of about 20 d before starting a declining trend toward the initial value, reached again after $\sim$100 d of the transient evolution. The rising phase is well fitted by the function $R_{\rm BB} = v (t - t_0)^\alpha$ as shown with a magenta dashed line in the bottom panel of Fig. 3. In particular, we fixed the initial time to $t_0 = -6.6 \pm -2.6$ d, which is the value obtained from the pseudo-bolometric luminosity, and we obtain power law with index $\alpha = 0.84 \pm 0.04$ and an expansion velocity $v = 4974 \pm 578$ km s^{-1}. It is interesting to note that the expansion phase of the BB radius last more days with respect to the rise of the luminosity, with the luminosity reaching the peak plateau well before the the reaching of the maximum value of the BB radius.

The photometric properties shown so far, such as the power-law rise to the peak luminosity in about 20 d, the power-law decay well resembling the $t^{-5/3}$ behaviour, the constant BB temperature at $T_{\rm BB} \sim 1.55 \times 10^4$ K but with an evolving BB radius, are all commonly observed in TDEs (Hinkle et al. 2020; van Velzen et al. 2020, 2021; Zabludoff et al. 2021, and reference therein), and thus they support the TDE nature of AT 2022wtn.

4 THE SPECTROSCOPIC FEATURES

In the following, we describe the spectroscopic analysis performed on the reduced spectra of AT 2022wtn with the aim to investigate on the transient's emission-line properties and evolution. The reduced spectra have been first corrected for foreground extinction by using the Cardelli law (Cardelli, Clayton & Mathis 1989) with $E(B - V) = 0.0651$ mag and assuming a reddening law with $R_V = 3.1$ (Schlafly & Finkbeiner 2011). Given the lack of an archival spectrum of the host galaxy and the presence of broad features related to the transient emission in the latest spectra we have, the analysed spectra are not host-subtracted. However, we have removed the contribution of the transient blue continuum by modelling it with a third-order SPLINE3 with the IRAF task `continuum`. We remark that, as emerged in the late-time spectra, the host galaxy has strong star-forming emission lines which, although narrow, could affect or even mask the presence of faint broad TDE lines, particularly in the low S/N spectra.

4.1 The emission-line fit

The emission lines detected in the continuum-corrected spectra are modelled by using a Gaussian function with the PYTHON fitting packages CURVEFIT and LEASTSQ. In the case of line profiles characterized by the simultaneous presence of more features (i.e. both broad and narrow components), a multicomponent Gaussian model has been used. During the fitting procedure a wavelength window of $\sim$1000 Å around the the spectral features of interest has been selected in order to include also the local continuum. The properties of the different components, such as the central wavelength (λ_c) and the full width at half maximum (FWHM), have been left as free parameters. In Fig. 5, we show the results (fit and residuals with respect to the model) for the He II + Hβ and the He I + Hα regions of the spectra taken at
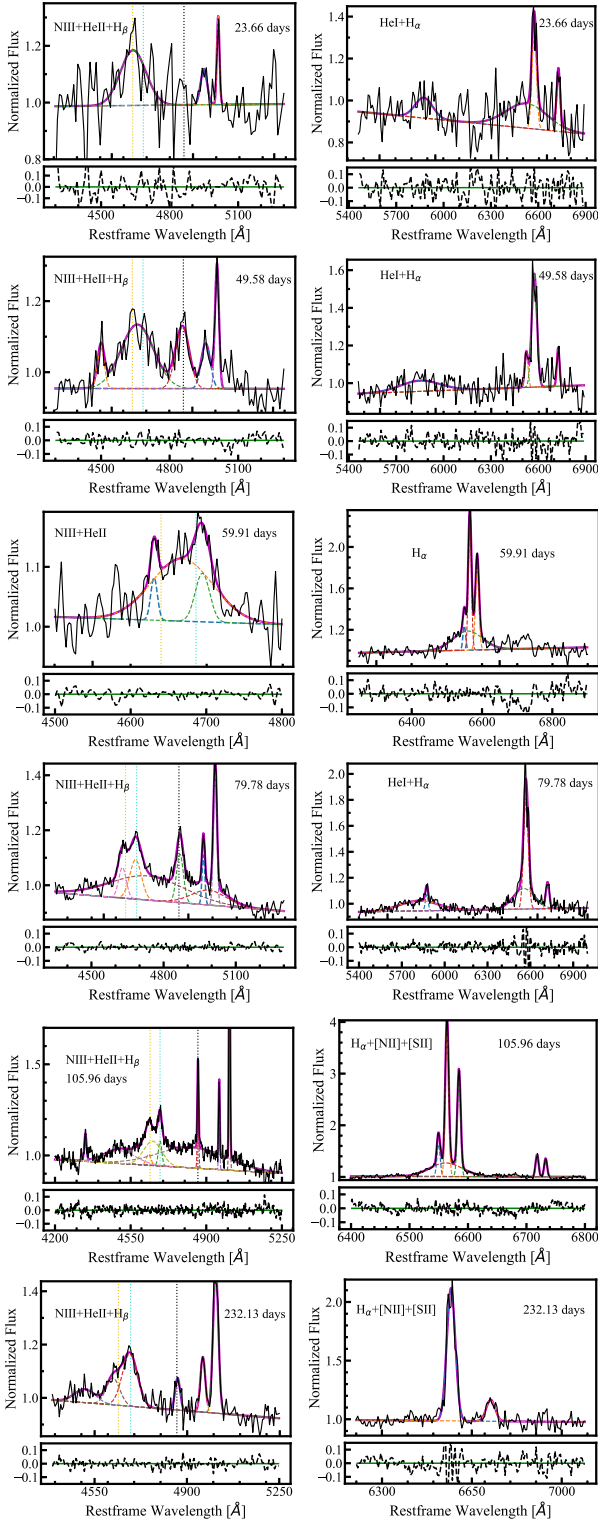
Figure 5. Results from the AT 2022wtn emission lines fit in the He II + Hβ and He I + Hα regions (left and right panels, respectively) for six different phases: 23.66, 49.58, 59.91, 79.78, 105.96, and 232.13 d from the transient discovery. Starting from 105.96 d no He I broad component is found. The Gaussian components are shown with dashed coloured lines, while the total model is represented with the magenta solid line. At the bottom of each panel, the residuals with respect the fitting model are shown. The location of the N III λ4640, He II λ4686, and Hβ is marked with the coloured dotted vertical lines (orange, cyan, and black, respectively).

23.66, 49.58, 59.91, 79.78, 105.96, and 232.13 d from the transient discovery. In Table A1, we report the fitting parameters [λ_c, FWHM, and the equivalent width (EW)] derived for the N III, Hydrogen, and Helium emission lines for each spectrum.

4.1.1 The spectroscopic evolution

The first spectrum, taken with SEDM 4.98 d after the transient discovery, shows only a blue continuum and some narrow emission lines, such as the Hβ, [O III] λ5007, Hα, and the [S II] λλ6716,6730 doublet blend which we ascribe to the host galaxy contribution. No broad components are clearly detected at this stage, however, we note that this is a low S/N spectrum, thus we could probably be not sensitive to the potential presence of broad but weak features.

A spectral evolution is seen in the subsequent sequence of spectra. Specifically, the spectra taken with LT/SPRAT at 23.66 and 49.58 d from the transient discovery (the first one it has been used for the spectroscopic classification, Fulton et al. 2022) show both broad and narrow emission lines (Fig. A1). In particular, broad components with FWHM $\sim 10^4$ km s^{-1} are found in correspondence of N III λ4640 and Hα, respectively, while a faint but well-centred broad component (FWHM ~ 6600 and $\sim 1.5 \times 10^4$ km s^{-1}, at 23.66 and 49.58 d, respectively) is detected at a position consistent with the He I λ5875. A faint Hβ appears at 23.66 d which intensify in the subsequent spectrum, where it is detected with an intermediate width of FWHM $\sim 4 \times 10^3$ km s^{-1}. We also note the emergence of a new emission line centred around $\lambda_c = 4503.46$ Å in the 49.58 d spectrum, which we tentatively identify with the N III λ4510. Instead, we do not detect any plausible feature in correspondence of the He II λ4686. We highlight that discriminating a broad N III λ4640 from a blueshifted He II λ4686 can be a difficult process due to their wavelength proximity (as shown in Nicholl et al. 2019) and requires spectroscopic observations with a resolution higher than that obtained with SPRAT. However, the fact that the broad N III λ4640 is well centred at the expected wavelength ($\lambda_c = 4641.77 \pm 7.27$ Å, see Table A1) and the evolution seen in the following spectra support this identification, although it is not conclusive in excluding any possible contribution of a He II component to the overall line profile.

Starting from 59.91 d from the transient discovery, we detect the emergence of a complex spectral feature composed by a series of different components in the He II λ4686 + Hβ region (see the left panels of Fig. 5). We clearly detect a broad feature (FWHM $\sim 6 \times 10^3$ km s^{-1}) at 59.91 d, still ascribable to the N III λ4640, although with a redshifted central wavelength ($\lambda_c = 4667.60 \pm 5.19$ Å). Furthermore, we observe the development of a clear He II λ4686 component as a double-horne shape in the N III λ4640 line profile (see Fig. 6). We note that this feature intensifies with time but it never develops a very broad component, keeping its width nearly constant at FWHM $\sim 4 \times 10^3$ km s^{-1} for all the time it is detected.

The evolution of the FWHM and the EW of all the broad and intermediate components detected in the AT 2022wtn spectral sequence are shown in the upper and bottom panels of Fig. 7, respectively. Specifically, we clearly detect broad components in the N III λλ4100, 4640 all showing an evolution with time of the FWHM, although reaching different values of the maximum width and with different timing (see the upper left panel of Fig. 7). In particular, both the N III λλ4100,4640 are still well detected at later times (393 d from the transient discovery) with FWHM $\sim 7 \times 10^3$ and $\sim 1.6 \times 10^4$ km s^{-1}, respectively. Instead, an intermediate-width He II λ4686 component is detected at later phases, after the luminosity peak, it never shows component exceeding the FWHM $\sim 4 \times 10^3$ km s^{-1} and it is
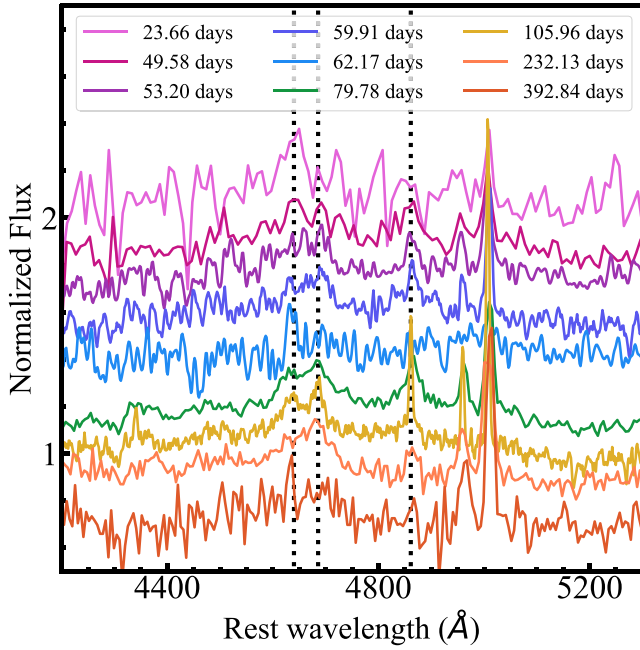
Figure 6. AT 2022wtn spectral evolution in the N III + He II $\lambda 4686$ wavelength region. Starting from 59.91 d from the transient discovery the appearance of two separate components ascribable to the N III $\lambda 4640$ and He II $\lambda 4686$ is clearly visible. Dotted vertical lines indicate the N III $\lambda 4640$, He II $\lambda 4686$, and Hβ position.

Figure 7. Upper panels: FWHM evolution of the broad components detected in the AT 2022wtn spectral sequence for the [N III] $\lambda\lambda 4100$ and 4640, and the He II $\lambda 4686$; the Hβ, He I $\lambda 5875$; and Hα (left and right panels, respectively). Middle panels: evolution of the central wavelength shift for the broad and intermediate components detected in the AT 2022wtn spectral sequence for the [N III] $\lambda 4640$, He II $\lambda 4686$, Hβ, He I $\lambda 5875$; and Hα (left and right panels, respectively). Bottom panels: EW evolution of the broad components detected in the AT 2022wtn spectral sequence for the [N III] $\lambda\lambda 4100$ and 4640 and the He II $\lambda 4686$; Hβ, He I $\lambda 5875$; and Hα (left and right panels, respectively). The coloured cross markers indicate the possible outflows components. The dashed grey vertical line shows the location of the VLA detection.

a long lasting feature (still detected in the last spectrum we have, taken at 393 d, upper left panel of Fig. 7).

In the upper right panel of Fig. 7 we show the FWHM evolution with time for the Helium and Hydrogen emission lines. Specifically, we detect broad/intermediate components in the Hβ, He I $\lambda 5875$, and Hα. Differently to what observed in the He II $\lambda 4686$, these others emission lines clearly show an evolution with time of their width. In particular, the He I $\lambda 5875$ and the Hβ are characterized by a widening trend, reaching maximum value for the line width of FWHM $\sim 2 \times 10^4$ km s^{-1} before disappearing, while the Hα shows narrowing trend. In any case, the broad components of all these lines are not detected anymore after ~ 100 d from the transient discovery.

The EW time evolution for the N III $\lambda\lambda 4100$, 4640 and for the He II $\lambda 4686$ are shown in the bottom-left panel of Fig. 7. We note that, while the N III $\lambda 4100$ feature show almost no time evolution of its EW, having a value of around 10 Å all the time, the EW of the N III $\lambda 4640$ shows an initial declining trend, starting from ~ 30 Å and reaching the value of ~ 10 Å only at 59.91 d, when He II $\lambda 4686$ is first detected. After this phase, no EW evolution is seen also for these two features. A possible explanation for the initial high values of the N III $\lambda 4640$ EW could reside in the blending of a faint and undetected He II $\lambda 4686$ component.

The identification of broad components of FWHM $\sim 10^4$ km s^{-1} in the N III and in the Hydrogen lines together with the observed spectroscopic evolution, are all compatible within the N-strong TDE scenario. The early detection of broad Bowen lines is a strong indication for the presence of a hidden accretion-related X-ray emission already ongoing, given that both a large flux of photons with $\lambda < 228$ Å and large optical depth in the obscuring/reprocessing photosphere (providing a multiple scattering regime) are needed in order to efficiently trigger the Bowen fluorescence mechanism, as outlined in Leloudas et al. (2019). In this scenario, the broadening of the Bowen lines is primarily due to the scattering process, their
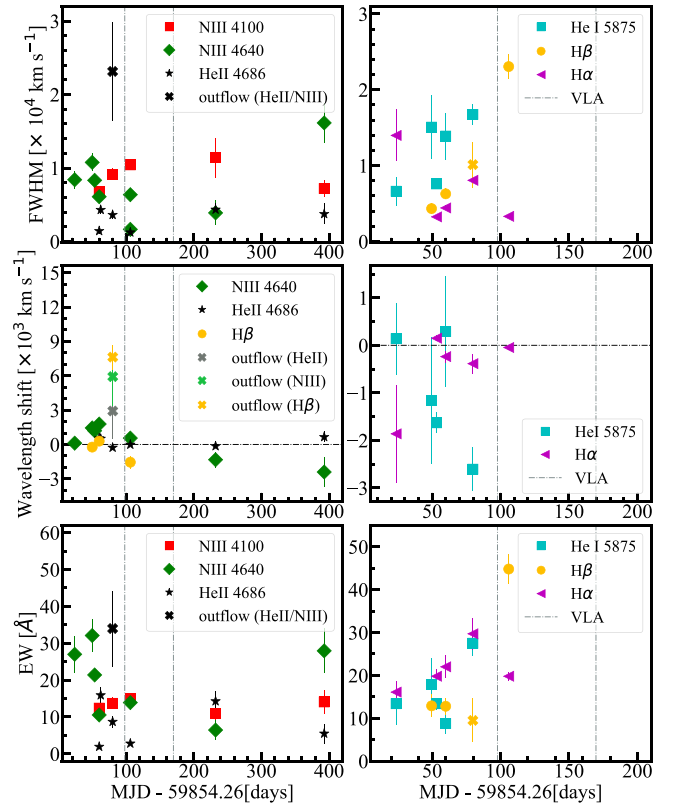
width depends on the system viewing angle (the wider the line the more edge on the system is observed, Dai et al. 2018) and a narrowing trend with time of the FWHM is consistent with the decreasing of the optical depth of the line-emitting region (Roth & Kasen 2018). Thus, in the case of AT 2022wtn, the non-detection of X-ray emission from the XRT monitoring coupled with the identification of very broad N III lines in the early spectra are consistent with an accretion powered X-ray-faint TDE viewed closer to the disc.

4.1.2 The presence of outflows

Beside the detection and the observed evolution of the broad features described before, we also detect a strong evolution in the measured central wavelengths for some of them together with the presence of two very broad components in the He II $\lambda 4686$ + Hβ region, which can be explained with the presence of an outflow.

In the central panels of Fig. 7, we show the evolution of the wavelength shifts with respect to the expected wavelength value for the broad/intermediate components detected in the N III $\lambda 4640$, He II $\lambda 4686$, Hβ, He I $\lambda 5875$, and Hα emission lines. In particular, the broad N III $\lambda 4640$ is first detected with a central wavelength consistent with the rest-frame value ($\lambda_c \sim 4641$ Å), however it subsequently

shows a gradual wavelength shift which first moves toward the red, reaching a maximum velocity shift of $v \sim 2 \times 10^3$ km s^{-1} measured at ~ 60 d, and then it shifts back toward the blue wavelengths, reaching a final velocity shift of $v \sim -2 \times 10^3$ km s^{-1} at 293 d. The intermediate component in the He II $\lambda 4686$ instead is always detected with a central wavelength consistent with its expected rest-frame value. Strong wavelength shift are also detected both in the Hα and in the He I $\lambda 5875$ broad components. Specifically, the broad Hα is detected at early times with a blueshifted central wavelength, corresponding to a velocity shift of $v \sim -2 \times 10^3$ km s^{-1} and, as it narrows, it progressively come back the expected central wavelength values. On the contrary, the He I $\lambda 5875$ broad component is first detected at zero wavelength shift and, while broadening, it progressively show a blueshift, reaching a final velocity shift of $v \sim -3 \times 10^3$ km s^{-1} at 79.78 d, before disappearing. These lines velocity offsets identified in AT 2022wtn are particular interesting as they can be used to probe the kinematics of the line forming region. Similar features in the emission lines have been already detected in a number of TDEs and, in some cases, have been attributed to the presence of outflows (Nicholl et al. 2020; Charalampopoulos et al. 2022). Moreover, a time evolution in the velocity shift is predicted in the framework of the Roth & Kasen (2018) model on the electron scattering effects in shaping the profiles of the lines emitted in an hot and outflowing reprocessing photosphere. Thus, the properties observed in the AT 2022wtn emission lines are consistent with being emitted in an outflowing reprocessing photosphere surrounding the SMBH.

Another indication for the presence of an outflow is represented by the additional very broad feature detected in the He II + Hβ region in the spectrum taken at 79.78 (see the central left panels of Fig. 5). Specifically, it is detected at a central wavelength $\lambda_c = (4731.68 \pm 38.88)$ Å (marked with a grey/green cross in the central left panel of Fig. 7) and with an FWHM $\sim 2.3 \times 10^4$ km s^{-1} (marked with a black cross in the upper right panel of Fig. 7). Given the complexity of this wavelength region, which at this stage is characterized by the simultaneous presence of many intermediate, broad, and narrow components, it is difficult to give a secure interpretation for this feature. However, if we assume that it is real, it will results in very broad component detected with a strong redshift ($v \sim 3 \times 10^3$ km s^{-1} if identified with the He II $\lambda 4686$, or $v \sim 6 \times 10^3$ km s^{-1} if instead we ascribe this feature the the N III $\lambda 4640$, grey cross and light green cross in Fig. 7, respectively). Although we cannot be confident about whether this component is real, if it is real and associated with either He II $\lambda 4686$ or the N III $\lambda 4640$ it could be interpreted as further evidence for an outflow. This interpretation is strengthened by the detection of a similar feature in the Hβ in the same spectrum (yellow cross in Fig. 7) and by the subsequent radio detection with the VLA (grey dashed vertical lines in Fig. 7).

5 THE HOSTING ENVIRONMENT

In this section, we analyse the properties of the whole hosting environment of AT2022wtn, including the neighbour galaxy in interaction, which makes this environment particularly interesting for the case of a TDE.

5.1 The SED fitting

In order to model the SED for each galaxy, we used the archival photometry reported in Table 1. Specifically, because of resolution and blending issues between the two neighbouring galaxies, the host of AT 2022wtn SED has been fitted by using only the archival SDSS (DR16) data, while for the neighbouring galaxy, SDSS J232323.37 + 104101.7, we have been able to use also the Two Micron All Sky Survey (2MASS, Skrutskie et al. 2006) archival photometry.

The SED has been modelled using the stellar population synthesis models in PROSPECTOR (Leja et al. 2017), which allow us to derive key physical parameters for both galaxies. In our fitting procedure, we left as free parameters the stellar mass, the metallicity, a six-component non-parametric star formation history (SFH) and dust parameters that control the fraction and reprocessing. The SFH parameters include the specific star formation rate (sSFR) and the widths of five equal mass bins used to compute the SFH. The results for both galaxies, including the best-fitting models, the photometry, and the median SFH profiles, are shown in Fig. 8. Specifically, for the AT 2022wtn host, we find a stellar mass of $\log(M_\star/M_\odot) = 10.29^{+0.12}_{-0.14}$, a metallicity of $\log(Z/Z_\odot) = -1.06^{+0.78}_{-0.60}$, and a specific star formation rate in the last 50 Myr of $\log(\text{sSFR}) = -11.53^{+1.21}_{-1.30}$. Comparably, for the neighbouring interacting galaxy, SDSS J232323.37 + 104101.7, we find a higher stellar mass of $\log(M_\star/M_\odot) = 11.09^{+0.11}_{-0.12}$, a metallicity of $\log(Z/Z_\odot) = -0.42^{+0.36}_{-0.57}$, and a specific star formation rate in the last 50 Myr of $\log(\text{sSFR}) = -11.96^{+1.31}_{-1.00}$. In the insert panels of Fig. 8, we show the weighted median SFR of each age-bin (black) and the 16th and 84th percentiles of model draws (shaded) derived from the fit versus the lookback time since the big bang for both galaxies.

We find that at the peak of the distribution the AT 2022wtn host galaxy is characterized by lower values of the SFR ($\sim 2\,M_\odot\,\text{yr}^{-1}$) with respect to the case of SDSS J232323.37 + 104101.7 ($\sim 10\,M_\odot\,\text{yr}^{-1}$). Moreover, both galaxies show a large drop in SFR in the last $\sim$Gyr, which is consistent with what found in other TDE hosts.

5.2 The galaxies emission lines

Given the peculiar hosting environment of AT 2022wtn, we obtain also a total of two spectra of the neighbour galaxy SDSS J232323.37 + 104101.7 (see Table 2), shown in Fig. 9 in comparison with the LRIS spectrum of AT 2022wtn, taken at 105.96 d from the transient discovery. In both the SDSS J232323.37 + 104101.7 optical spectra Hα and [S II] doublet narrow emission lines are well detected. However, the [S II] doublet is not deblended, while only in the DeVeny spectrum the Hα is well separated from the [N II] $\lambda 6583$. Thus, we used the Hα in order to measure the redshift of this galaxy. We obtained a $z = 0.048 \pm 0.01$, which is consistent with that of AT 2022wtn.

Overall, the two galaxies appear of a quite different nature, with the bigger one SDSS J232323.37 + 104101.7 showing a face-on elliptical morphology (as deduced from visual inspection in the Legacy Survey image, shown in Fig. 1) and a quite passive spectrum with only the Hα, [N II], and [S II] lines detected in emission. Instead, although still contaminated by the TDE emission in the blue part of the spectrum, the AT 2022wtn host galaxy is characterized by the presence of a number of narrow emission lines, ascribable to the host environment. In particular, the LRIS spectrum is the one with the highest resolution we have, and, thus, it has been possible to deblend the narrow emission lines used for the BPT diagrams (Baldwin, Phillips & Terlevich 1981). In Section 4, we describe the multi-Gaussian fitting procedure applied on the continuum-subtracted spectra of AT 2022wtn. The same method has been used in the case of the LRIS spectrum, where both the TDE broad lines and the host galaxy narrow emission lines have been modelled separately (see Fig. 5). From the derived EW of the relevant lines for the BPT diagnostic diagram we obtain the following ratios: $\log_{10}(\text{[N II]}6583/\text{H}\alpha) = -0.19 \pm 0.026$; $\log_{10}(\text{[O III]}5007/\text{H}\beta)$
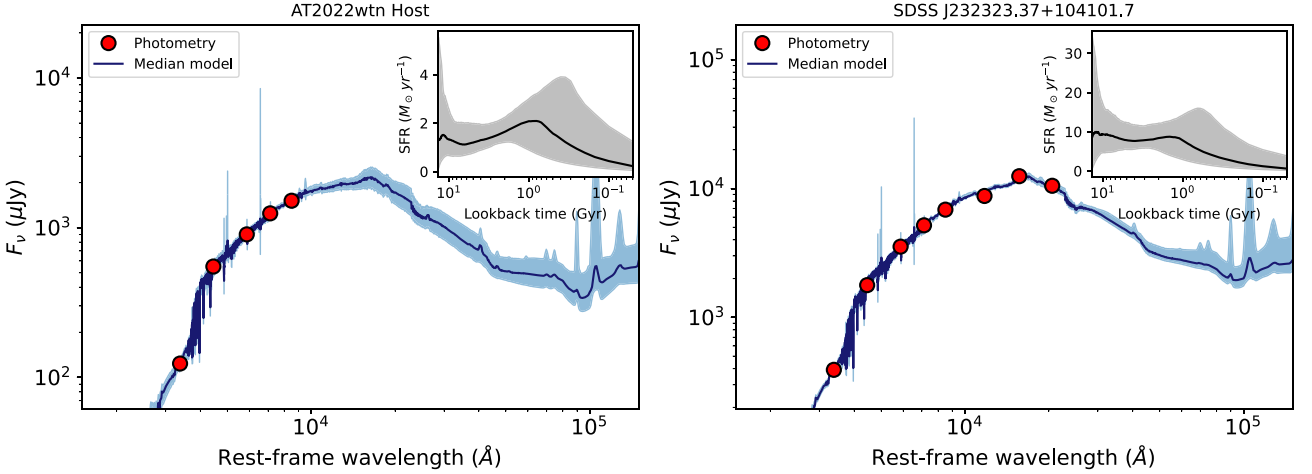
Figure 8. Results from the PROSPECTOR modelling for both the AT 2022wtn host and the interacting galaxy, SDSS J232323.37 + 104101.7 (left and right panels, respectively). The main figures show the archival photometry (red filled circles) and the best-fitting SED model (blue) with 16th and 84th model distribution percentiles (shaded). The subplots, show the derived median SFH (black) and 16th and 84th percentiles (shaded).
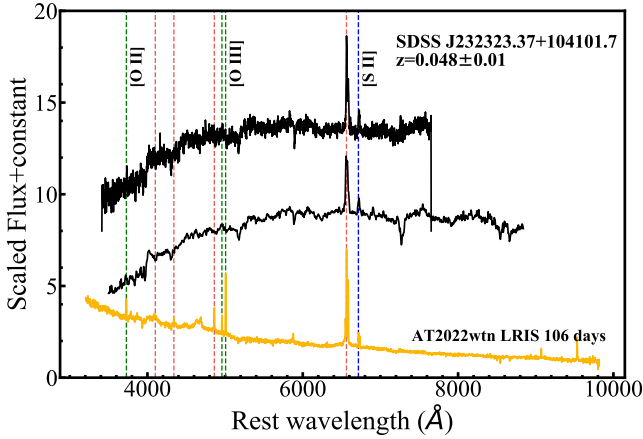

Figure 9. Spectra of the neighbouring and interacting galaxy SDSS J232323.37 + 104101.7 (in black) in comparison with the AT 2022wtn LRIS spectrum, taken after 105.96 d from the transient discovery (in yellow). The two galaxies are at a compatible redshift. Vertical coloured dashed lines show the position of the main emission lines at this redshift: Hydrogen (red), Oxygen (green), and the [S II] doublet.

$= 0.43 \pm 0.06$ and $\log_{10}([\text{S II}]6716,6731/\text{H}\alpha) = -0.62 \pm 0.08$. In Fig. 10, we show the position in the BPT diagnostic diagrams of AT 2022wtn. For comparison, we show also the results for some TDEs for which line ratios are available in literature: OGLE16aaa (Wyrzykowski et al. 2017); PS16dtm (Blanchard et al. 2017); SDSS J0159 + 0033 (Merloni et al. 2015); SDSS J0748; ASASSN-14ae; ASASSN-15li; PTF09djl; PTF09ge (French et al. 2017); iPTF16fnl (Onori et al. 2019); and AT 2017gge (Onori et al. 2022). The line ratios derived for AT 2022wtn place its host galaxy slightly above the separation line between the composite and the AGN area and slightly below the separation line between the star-forming and the Seyfert galaxies. Although at this phase, the contribution of the TDE emission features is non negligible, this is still a strong indication of a non-passive nature of the AT 2022wtn host galaxy, possibly a star-forming environment, which is known to be enriched in gas and dust. Thus, similarly to what has been observed in the TDE AT 2017gge and AT 2019qiz (Onori et al. 2022; Short et al. 2023),
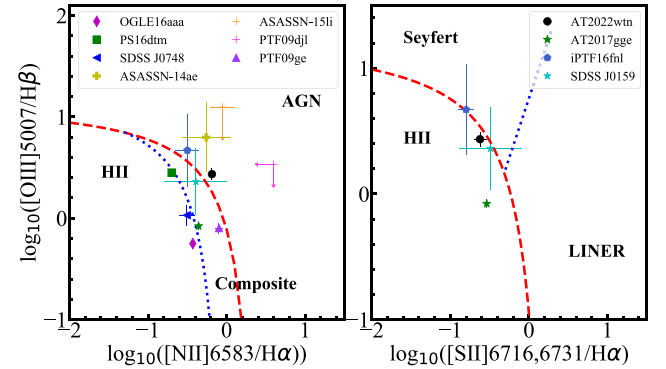

Figure 10. BPT diagrams for the host of AT 2022wtn. We used the EWs of the narrow emission lines detected in the late-time Keck spectrum which we ascribe to the host environment (black filled point). The different activity regions of the diagram are separated by the following lines: red dashed line from Kewley et al. (2001), blue dotted line from Kauffmann et al. (2003) in the left panel and blue dotted line from Kewley et al. (2006) in the right panel. For comparison, we also show the position of some TDE host galaxies: OGLE16aaa (Wyrzykowski et al. 2017); PS16dtm (Blanchard et al. 2017); SDSS J0159 + 0033 (Merloni et al. 2015); SDSS J0748; ASASSN-14ae; ASASSN-15li; PTF09djl; and PTF09ge (French, Arcavi & Zabludoff 2017); iPTF16fnl (Onori et al. 2019); and AT 2017gge (Onori et al. 2022).

a late-time development of high ionization coronal emission lines could be observed in future spectroscopy.

5.3 Properties of the neighbouring galaxy SDSS J232323.37 + 104101.7

Fig. 11 shows the PPXF[9] analysis of the neighbouring galaxy's DeVeny spectrum, having approximate an instrumental resolution of $R \sim 2000$ (i.e. $\sim 190 \text{ km s}^{-1}$). The upper panel represents the

---

[9]This is a PYTHON implementation of the Penalized PiXel-Fitting method to perform full-spectrum fitting to extract the stellar and gas kinematics, as well as the stellar population of stars and galaxies (Cappellari 2017, and references therein).
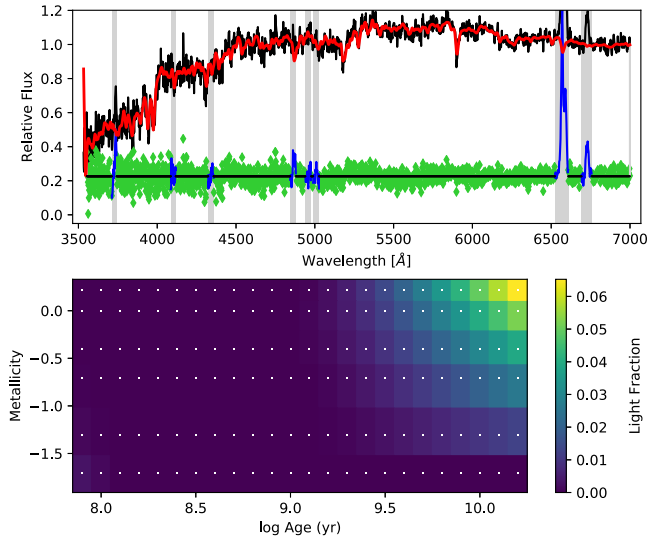
Figure 11. PPXF modelling of the spectrum of neighbouring galaxy SDSS J232323.37 + 104101.7.

stellar and gas kinematics, showing the modelled stellar component (red curve) of the observed galaxy spectrum, corrected for redshift and galactic reddening (black curve). The galaxy emission regions have been masked (marked as shaded vertical regions) while fitting the model spectra. Green (blue) points (curves) are residuals of the fitted (masked) regions. The model stellar component is a weighted average of the spectra taken from the Miles stellar libraries (Sánchez-Blázquez et al. 2006; Falcón-Barroso et al. 2011). The computed value of stellar velocity dispersion through PPXF fit is 310 ± 38 km s^{-1}. Following the prescription of Ferrarese & Ford (2005), this corresponds to a BH mass of $\log(M_{\mathrm{BH}}/M_{\odot}) = 9.15^{+0.39}_{-0.41}$. The lower panel shows the distribution of the weights of the model components in the phase space of stellar age and metallicity. The weighted-average value of the stellar age of the system is of $\log(\mathrm{age/year}) \sim 9.85$, and the weighted-average metallicity is ~ -0.2 consistent with the results presented in Section 5.1.

We used the luminosity of the Hα emission line of the residual spectrum to compute the neighbouring galaxy's current SFR. The measured value of Hα emission line (after deblending from [NII] $\lambda\lambda 6548$, 6584, and applying galactic extinction correction) is $(2.66 \pm 0.2) \times 10^{-14}$ erg s^{-1} cm^{-2}. This corresponds to an Hα luminosity of $(15 \pm 1) \times 10^{40}$ erg s^{-1}. This indicates a current SFR of 1.2 ± 0.8 M$_{\odot}$ yr^{-1} (Kennicutt 1998, and references therein).

6 THE BLACK HOLE MASS ESTIMATION

In order to derive the mass of the BH involved in this TDE, we used two independent methods available in literature: modelling the multiband light curves with the Modular Open Source Fitter for Transients (MOSFIT, Guillochon et al. 2018) and the TDEMASS tool (Ryu, Krolik & Piran 2020). These two approaches are based on different assumptions about the main optical emission mechanism. In particular, MOSFIT assumes that the energy generation is proportional to the instantaneous mass fallback rate (but is agnostic to the mechanism that converts this to radiation), while TDEMASS considers the UV/optical light production as powered by shocks between intercepting stellar debris streams near the apocentres of the debris orbits.
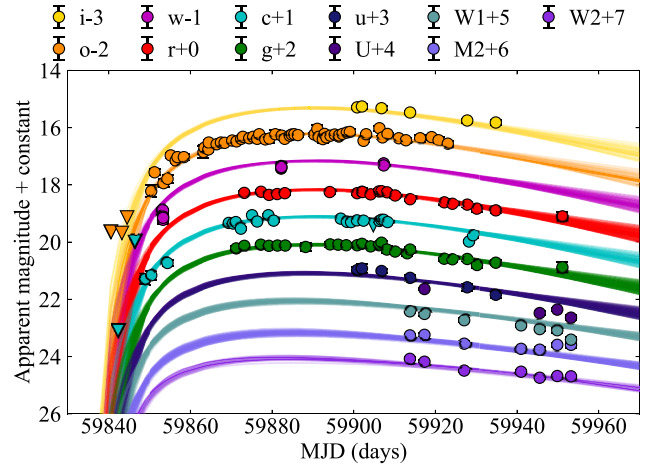

Figure 12. MOSFIT fit of the AT 2022wtn multicolours light curves.

In the following, we describe the results obtained by using each method.

6.1 The multicolour light curves fit with MOSFIT

We derive the physical parameters of the stellar disruption by fitting the host-subtracted multiband light curves of AT 2022wtn by using MOSFIT and the TDE model described in Mockler et al. (2019), which assume that the rate of energy generation is proportional to the stellar debris fallback rate, whose time evolution is taken from the simulations of Guillochon & Ramirez-Ruiz (2013). More specifically, MOSFIT uses scaling relations and interpolations for a range of encounter parameters and masses for the BH and for the disrupted star. It generates both a bolometric light curve and multiband light curves, which are in turn fitted to the observed data. Finally, it gives as output the combination of the highest likelihood match parameters. The fits to the AT 2022wtn multicolours light curves are shown in Fig. 12. The model represents quite accurately the photometric measurements, except for the late-time epochs (around MJD 59 950), where the transient is too faint and it almost reached the host level. We find a SMBH mass of $M_{\mathrm{BH}} = 1.2 \pm 0.2 \times 10^6$ M$_{\odot}$ and a very low mass for the disrupted star of $M_{\star} = 0.09 \pm 0.02$ M$_{\odot}$. Additionally, we found a scaled impact parameter $b = 1.32^{+0.19}_{-0.16}$ which is consistent with a full stellar disruption (for $b > 1$, see Mockler et al. 2019, for details). Finally, the free parameters of the model, their priors and their posterior probability distributions are reported in Table 3, while the two-dimensional posteriors are shown in Fig. B1. We note that the posteriors on ε peaks at ~ 4 per cent, which is below the canonical accretion efficiency of ~ 10 per cent. A possible explanation is that suggesting that a substantial fraction of the stellar mass may not be accreted, which could be connected to the radio detection.

6.2 The TDEMASS fit

TDEMASS is a new method, recently proposed by Ryu et al. (2020) in order to infer the mass of the disrupted star and of the SMBH by using only two input quantities: the UV/optical luminosity and the colour temperature at the peak of the flare. Differently to MOSFIT, this tool is based on the physical model of Piran et al. (2015) in which the UV/optical emission originates in the outer shocks that form during the intersections of the stellar debris streams near their orbital apocentre. For the case of AT 2022wtn, we used as input for the peak

Table 3. Priors and marginalized posteriors for the MOSFIT TDE model. Priors are flat within the stated ranges, except for M_*, which uses a Kroupa initial mass function. The quoted results are the median of each distribution, and error bars are the 16th and 84th percentiles. These errors are purely statistical; Mockler, Guillochon & Ramirez-Ruiz (2019) provide estimates of the systematic uncertainty.

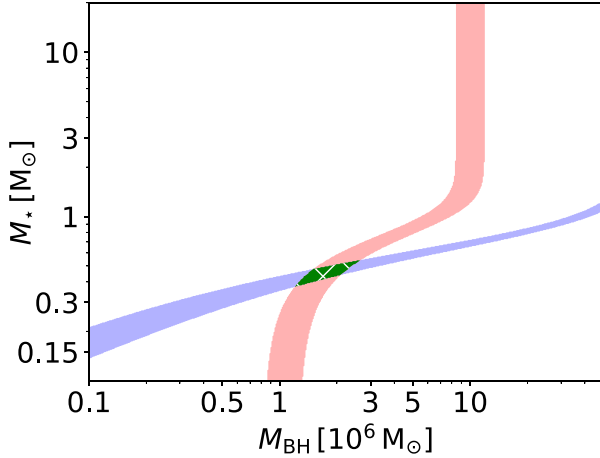| Parameter	Prior	Posterior	Units
$\log(M_{\bullet})$	[5, 8.7]	$6.06^{+0.08}_{-0.09}$	$M_{\odot}$
M_*	[0.01, 100]	$0.09^{+0.01}_{-0.02}$	$M_{\odot}$
b	[0, 2]	$1.32^{+0.19}_{-0.16}$	
$\log(\epsilon)$	[−4, −0.4]	$-1.42^{+0.16}_{-0.17}$	
$\log(R_{\mathrm{ph},0})$	[−4, 4]	$1.15^{+0.23}_{-0.24}$	
l_{ph}	[0, 4]	$2.39^{+0.46}_{-0.48}$	
$\log(T_v)$	[−3, 5]	$1.23^{+0.09}_{-0.20}$	d
t_0	[−500, 0]	$-14.56^{+1.96}_{-2.02}$	d
$\log(n_{\mathrm{H,host}})$	[16, 23]	$21.02^{+0.04}_{-0.06}$	cm^{-2}
$\log\sigma$	[−3, 2]	$-0.95^{+0.03}_{-0.03}$	

Figure 13. The inferred solutions for the M_{BH} and $M_{\star}$ found by using the TDEMASS tool fot AT 2022wtn. The blue strip indicates the solutions for the given value of the peak luminosity, while the red strip shows the solution for the given temperature input. The green region indicates the solutions found for both inputs.

luminosity the average of the L_{BB} values during the plateau phase of the TDE peak ($<L_{\mathrm{BB,max}}> = 1.4\pm0.2 \times 10^{43}$) erg s^{-1} and the corresponding averaged temperature ($T_{\mathrm{BB}} = 1.4 \pm 0.1 \times 10^4$ K) for the colour temperature input. Following the tool's recommendation, we run the code keeping fixed the parameters c1 and del_omega to the default values. By using this independent method, we obtain the following output parameters: $M_{\mathrm{BH}} = 1.7^{+0.9}_{-0.5} \times 10^6$ $M_{\odot}$ and $M_{\star} = 0.46 \pm 0.09$ $M_{\odot}$ for the mass of the BH and the disrupted star, respectively, the characteristic mass return time of the most tightly bound debris $t_0 = 57^{+21}_{-15}$ d and the apocentre distance $a_0 = 10^{+4}_{-3} \times 10^{14}$ cm. In Fig. 13, the inferred solution found for the M_{BH} and $M_{\star}$ are shown. Interestingly we obtain with MOSFIT a compatible value for the BH mass ($M_{\mathrm{BH}} = 1.2\pm0.2 \times 10^6$ $M_{\odot}$), while, as expected from the comparison study presented in Ryu et al. (2020), a smaller mass for the disrupted star ($M_{\star} = 0.09 \pm 0.02$ $M_{\odot}$).
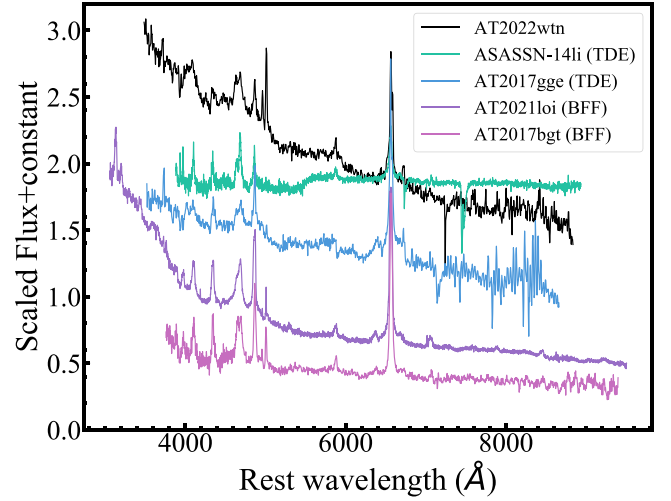

Figure 14. Comparison between the AT 2022wtn spectrum taken at 79.78 d and the optical spectra, the TDEs AT 2017gge (Onori et al. 2022) and ASASSN-14li (Holoien et al. 2016a) and the BFFs AT 2017bgt (Hosseinzadeh et al. 2017) and AT 2021loi (Graham & Scott 2013).

7 DISCUSSION

7.1 The TDE nature of AT 2022wtn

Our multiwavelength follow-up campaign dedicated to the transient AT 2022wtn and covering ∼393 d from its discovery, enlightened a number of observable properties all compatible with a TDE nature. Specifically, its location is consistent with the nuclear region of the galaxy SDSS J232323.79 + 104107.7 (which is undergoing a merger with the more massive galaxy SDSS J232323.37 + 104101.7), the UV/optical light curve is characterized by a rising phase of ∼20 d, a decline consistent with the TDE models and, as found from the photometric analysis, maximum luminosity of $<L_{\mathrm{BB,max}}> = 43.13 \pm 0.06$ erg s^{-1}, and a nearly constant temperature of $T_{\mathrm{BB}} \sim 1.55 \times 10^4$ K.

The X-ray non-detection derived from the *Swift*/XRT telescope monitoring, placed AT 2022wtn among the optically selected and X-ray faint TDE population, while the detection of broad components (FWHM $\sim 10^4$ km s^{-1}) in the Hα, He I λ5875, and N III λ4640 in the early spectra, suggests it can be classified as a Bowen TDE-H + He subclass. The most noticeable spectroscopic feature is the formation of the N II λ4640 + He II λ4686 double horned broad line, clearly visible starting from 59.91 d from the transient discovery. Such feature is commonly observed in the class of the Bowen Fluorescence Flare (BFF) nuclear transients, recently associated to an enhanced accretion in active SMBHs (Tadhunter et al. 2017; Makrygianni et al. 2023). In Fig. 14, we show a comparison between the AT 2022wtn spectrum taken at 79.78 d and the optical spectra the two TDEs showing a similar double-horned spectral features in the He II λ4686 region, AT 2017gge (Onori et al. 2022) and ASASSN-14li (Holoien et al. 2016a), and two BFFs, AT 2017bgt (Hosseinzadeh et al. 2017; Trakhtenbrot et al. 2019) and AT 2021loi (Graham et al. 2021; Makrygianni et al. 2023). This spectral similarity suggests that at least some of BFFs could indeed produced by a TDE-induced rejuvenated accretion onto an active SMBH.

We estimate the physical parameters of the disruption by using two independent methods: by fitting the multiband host-subtracted light curve with MOSFIT and by using the TDEMASS package. From both methods, we find compatible values for the mass of

the SMBH ($M_{BH;MOSfit} = (1.2 \pm 0.2) \times 10^6$ M$_\odot$ and $M_{BH;TDEmass} = 1.7^{+0.9}_{-0.5} \times 10^6$ M$_\odot$) leading to an Eddington ratio range of $\lambda_{Edd} = 0.06$–0.09 (i.e. hence a sub-Eddington accretion). In addition, the MOSFIT analysis indicates the occurrence of a full disruption of a low-mass star ($M_\star = 0.09 \pm 0.02$ M$_\odot$), while the the TDEFIT results indicate a higher mass of the disrupted star, but sill sub-solar ($M_\star = 0.46 \pm 0.09$). Interestingly, the low-mass value of the MOSFIT $M_\star$ could be explained within a scenario in which a substantial fraction of the stellar debris is not accreted because of the presence of outflows, which, in turn, causes radio emission detected at later times.

We note that finding TDEs in interacting pair of galaxies is particularly interesting given the possible implications on the rate of TDEs in merging and post-merging hosting galaxy (see the results from Wevers & French 2024), which we discuss in Section 7.4. It appears that as a consequence of the TDEs discovery rate increasing, thanks to the development of more efficient transient dedicated surveys, we are able to enrich the TDE sample with transients in such a peculiar environments. Indeed, another confirmed TDE (AT 2023clx, Charalampopoulos et al. 2024) plus some TDE candidates (Mattila et al. 2018; Kool et al. 2020; Reynolds et al. 2022; Payne et al. 2023) have been recently discovered hosted in merging galaxies.

Besides the observed typical TDE features, a number of interesting peculiarities have been also unveiled both from the photometric and the spectroscopic analysis which are discussed in the following subsections, with the aim to derive clues on the TDE emission mechanism and the properties of the emitting region.

7.2 A TDE with a maximum luminosity plateau and a dip in the temperature

The first peculiar feature of AT 2022wtn consists of a 30 d long peak in which the luminosity remains at its maximum value ($<L_{BB,max}> = 43.13 \pm 0.06$ erg s^{-1}, i.e. the maximum luminosity plateau phase). During this period, we observe a corresponding decrease in the temperature, which drops to $T_{BB} \sim 1.35 \times 10^4$ K, and remains nearly constant around this value for all the duration of the maximum luminosity plateau phase. When the luminosity starts declining, it rises again to the initial value of $T_{BB} \sim 1.55 \times 10^4$ K. These trends are accompanied by a fast expansion of the radius of the photosphere, characterized by a velocity of $v \sim 5000$ km s^{-1} and a steep rise to the maximum ($R_{BB} \sim 9 \times 10^{14}$ cm). Although steeper than the luminosity rising phase, the photosphere expansion last more days, with the radius reaching its maximum value around 10 d after the beginning of the maximum luminosity plateau. Interestingly, during this phase, we detect in the spectra only the N III, the Hα and, similar to AT 2023clx (Charalampopoulos et al. 2024), the He I λ5875 broad/intermediate emission lines. It is only after $\sim$10 d from the start of the luminosity decline, when the temperature is already back to its initial value and the photospheric radius shrinks, that the broad/intermediate components in the He II λ4686 and the Hβ appear in the spectra. However, we stress that, given the very low spectral resolution of the early spectra, we may be not sensitive to the presence of a faint He II λ4686 component in blend with the stronger and broad N III λ4640.

We note that a velocity of the expanding photosphere of $\sim$5000 km s^{-1} is quite fast with respect to what derived for others TDEs [specifically 2200 km s^{-1} (AT 2019qiz; Nicholl et al. 2020), 2900 km s^{-1} (AT 2020zso; Wevers et al. 2022), and 1300 km s^{-1} (AT 2020wey; Charalampopoulos et al. 2023)], but it is similar to the case of AT 2023clx (Charalampopoulos et al. 2024). Another interesting similarity between these two TDEs is that also in AT 2023clx a 10–

30 d post-peak dip in temperature lasting about 30 d was observed in the photometric analysis, although there is no a corresponding maximum luminosity plateau phase. Moreover, unlike AT 2023clx, there is no NUV break detection in the AT 2022wtn light curves, we do not observe a double peak in the radius evolution and the rising phase of the light curve is slower.

Following the study of Wong, Pfister & Dai (2022) on the effects of disc formation efficiency in TDEs, Charalampopoulos et al. (2024) explained the photometric properties observed in AT 2023clx with a full disruption of a low-mass star and a prompt and efficient disc formation scenario. Given that also in the case of AT 2022wtn, the photometric analysis is compatible with the full disruption of a low-mass star, placing AT 2022wtn in similar condition for the efficiency of disc formation within the Wong et al. (2022) analysis, we suggests that also in this case an efficient circularization process took place and led to the prompt formation of an accretion disc. The non-detection of X-ray emission, but the identification of N III emission lines in the early spectra, coincident with the beginning of the maximum luminosity plateau phase, are a strong indication that EUV/X-ray photons are indeed emitted from the newly formed disc, but an edge-on view of the system prevents the X-rays detection (see the TDE unification model of Dai et al. 2018).

The energy released by the prompt circularization and accretion is also expected to be trapped in a promptly launched quasi-spherical envelope of outflowing material (i.e. a reprocessing photosphere responsible for the UV/optical emission) (Jiang et al. 2016; Metzger & Stone 2016; Lu & Bonnerot 2020; Roth et al. 2020; Metzger 2022). Interestingly, outflows models driven primarily by circularization predict a photospheric temperature evolution similar to the dip in temperature observed in AT 2022wtn (first declining and then, after the peak of the light curve, it rises again, see Roth et al. 2020, and reference threrein). Moreover, if the peak in the observed luminosity is powered by the trapped radiation which adiabatically transfers energy to the gas, a longer trapping phase may explain the observed luminosity plateau in AT 2022wtn. The contraction of the photospheric radius may mark the moment in which the mass fallback rate drops and the radiation finally can escape.

7.3 The spectroscopic evolution and the detection of outflows

Thanks to our promptly started spectroscopic follow-up campaign, we have been able to monitor the TDE evolution, since 5 d after the transient discovery, with the first spectrum taken during the rising phase of the light curve. It is interesting to note that broad components consistent with the TDE emission arise in the spectra only $\sim$20 d after the transient discovery, an epoch coincident with the beginning of the maximum luminosity plateau phase and the dip in the photospheric temperature. The broad features that are detected at this stage are in correspondence of the Bowen fluorescence line N III λ4640 (FWHM $\sim 8.4 \times 10^3$ km s^{-1}), the Hα (FWHM $\sim 14 \times 10^3$ km s^{-1}), and the He I λ5875 (FWHM $\sim 6.6 \times 10^3$ km s^{-1}), making AT 2022wtn classifiable as an N-strong TDE. It is only after the end of the maximum luminosity that we have been able to detect the He II λ4686 in the spectra, arising beside the N III λ4640 as a double-horn feature (its developments is shown in Figs 5 and 6). We also note that, in contrast to what is observed in the Hydrogen and N III lines, the He II λ4686 never reaches the typical width expected in the TDE broad features, it does not show velocity evolution, keeping a nearly constant width with values around FWHM $\sim 4 \times 10^3$ km s^{-1} during all its presence in the spectra, and it is a persistent feature, being still detected 392 d from the transient discovery (together with the

N III lines, see Fig. 7). Furthermore, as shown in Fig. 7, the detection of the He II λ4686 is soon followed by the disappearance of the He I λ5875.

A similar spectroscopic behaviour, coupled with a similar temperature evolution is peculiar, but not unique. Indeed it has recently been observed also in the TDEs AT 2018hyz and AT 2023clx (Gomez et al. 2020; Short et al. 2020; Charalampopoulos et al. 2024), where, in both cases, a temperature dip has been observed to be accompanied with the early presence of He I lines and a late-time emergence of the He II in correspondence of the temperature rising phase. However, it is worth noting that, unlike AT 2022wtn, in both these two TDEs, the pseudo-bolometric luminosity does not show a maximum luminosity plateau phase.

In the case of AT 2023clx, Charalampopoulos et al. (2024) ascribe the early presence of the He I to the temperature drop as it allows the He II to recombine into He I. As the temperature rises again He I gets ionized and the He II arises again. This explanation could work also for AT 2022wtn, although none of these features have been detected in the first spectrum. However, we note that we have no spectroscopic observations between 5 and 20 d, the spectrum taken at 5 d is at low S/N and the low resolution of the first three spectra could prevent us from de-blending a faint He II λ4686 component from the N III λ4640 broad line. Thus, it is possible, but not secure, that we are witnessing a late-time developing of the He II λ4686. However, independently from our capability to detect a possible faint He II in the early spectra, the recombination of the He I into He II after the temperature dip can still explain the He II increase in intensity at this stage as, after these epochs, we are able to de-blend its contribution from the N III even in the late-time low-resolution spectra).

In any case, as discussed in the Section 7.2, the AT 2022wtn photometric properties are consistent with an efficient circularization process, a prompt accretion disc formation and the launch of a quasi-spherical reprocessing envelope of fast expanding outflowing material. The non-detection of X-ray emission from the disc, coupled with the presence of Bowen lines in the early spectra, further support this scenario (with an edge-on viewing angle for this system), given that ionization of a reprocessing atmosphere by X-ray/EUV photons is needed in order to trigger the Bowen fluorescence mechanism. A variation in density and temperature in this expanding reprocessing photosphere could be responsible for the late-time detection of the He II.

Interestingly, Gomez et al. (2020) and Short et al. (2020) explain the properties of He II in the AT 2018hyz spectra either by the presence of an outflowing reprocessing material or due to a late-time shocks in debris collisions, with the He II produced in a region placed further out with respect to the Hydrogen lines, given that it shows a lower width, different line profile evolution with respect to the other emission lines and a late-time appearance. As discussed before, we observe similar He II properties also in the case of AT 2022wtn and, in addition, we have indications for the presence of a fast-expanding outflow. Indeed, as outlined in Section 4.1.2, we detect velocity offsets in the broad/intermediate components of Hydrogen, He I, and N III emission lines and two additional very broad features with strong redshift in the He II + Hβ region of the spectrum taken at 79.78 d. Given that these broad features are characterized by very complicated line profiles, we tentatively ascribe these components either to N III or He II and to Hβ, but we cannot be secure. However, their strong shift in wavelength coupled with the detection of a radio emission of transient nature consistent with the position of AT 2022wtn in the following days (Christy et al. 2023), strongly support an outflows origin for these features.

7.4 An interacting host: implications for the TDE rate

Since two TDEs – AT 2022wtn and AT 2023clx – out of the few tens of optically selected events have now been discovered in interacting galaxies, in this section we will discuss and estimate how much more frequently TDE host galaxies undergo mergers compared to the general population of similar galaxies. We note that in the IR also a number of events have been discovered in interacting pairs of galaxies and galaxy merges suggesting the presence of a dust-obscured population of TDEs therein (Mattila et al. 2018; Kool et al. 2020; Reynolds et al. 2022). However, in our discussion below we will focus only on optical TDEs.

A simplified method to derive such an estimation is quite straight-forward: assuming a sample size of approximately the number of known TDEs ($\sim$100) and assuming that only one TDE is in a galaxy with a double nuclei and interaction tails (i.e. AT 2022wtn), we can derive a frequency of such events of ~ 1 per cent. Using visual classification of a general population of galaxies, Bridge et al. (2010) found that the fraction of galaxies with double nuclei and tails is $\sim$0.1 per cent at low redshift ($z < 0.2$). This simple metric implies TDEs are 10 times more likely to be in this class of merger than the general galaxy population (i.e. a TDE boost factor of 10). Of course, finding a second TDE host in this stage, would increase the boost factor to 20, and shows that there is significant sampling uncertainty in this method due to the small number of known TDEs.

Alternatively, if we assume that AT 2022wtn is the only TDE in an interacting system, we can compare the 1 per cent frequency of TDEs in interacting systems to the observed merger fractions of galaxies. Typically, the observed merger fraction is measured by assuming that close pairs galaxies are bound, and will merge on some to be defined time-scale. In this framework, in order to derive an estimation of the boost TDE factor we would like to get a merger fraction per Gyr from the literature for the case of our mass and mass ratio galaxy and then compare that to the implied merger fraction from AT 2022wtn. Specifically for the case of AT 2022wtn, we have obtained the mass of both the two galaxies involved in the interaction from the SED fitting (see Section 5.1), which result to be $\log(M_\star/M_\odot) = 11.09^{+0.11}_{-0.12}$ for the primary galaxy (SDSS J232323.37 + 104101.7) and $\log(M_\star/M_\odot) = 10.29^{+0.12}_{-0.14}$ for the AT 2022wtn host. Thus, the mass ratio in this system is $\mu \approx 1/10$, making this a minor merger. According to Mundy et al. (2017), for system similar to the one hosting AT 2022wtn (minor merger and separations in the range 5 kpc $< r <$ 30 kpc), the minor merger pair fraction at $z = 0$ is 0.02. To turn this into a merger rate, we need to assume a time-scale for this merger to occur. For pairs with this separation and mass ratio, Conselice et al. (2022) find that the pair lifetime at $z = 0$ is 1.93 Gyr, which would give a merger rate per Gyr of 0.02/1.93 Gyr $= 0.010$ Gyr^{-1}. This is consistent with direct numerical simulations which suggest for the AT 2022wtn case a merger rate per Gyr of 0.007 (for a 1/4–1/10 merger of a 10^{10}–10^{11} M$_\odot$ primary galaxy; O'Leary, Moster & Krämer 2021).

Now, we can estimate the merger rate in the population of TDEs by assuming that only AT 2022wtn has a close companion. This is clearly a lower limit, and so will lead to a lower limit on the boost factor. AT 2022wtn is at redshift 0.049, which means the angular separation of 8.7 arcsec between the centres of the two galaxies is equivalent to 8.4 kpc. From the literature on numerical simulations, we can estimate the time-scale until AT 2022wtn completes the merger. Generally, the time-scales on which the kind of morphological features are seen are roughly $\sim$0.2–0.4 Gyr (Lotz et al. 2010; O'Leary et al. 2021). Notice that this is different from the time-scale of the previous paragraph because the tidal tails of the interacting galaxy live for a much shorter time.

We can determine how many galaxies should be merging in the TDE population if they are part of the general population, namely:

$$N_m = N_g * \Gamma_{\text{merg}} * \tau \qquad (1)$$

where N_m is the number of merger pairs, N_g is the number of galaxies in the sample, Γ_{merg} is the merger rate, and τ is the merger lifetime. If we assume a sample of TDEs (N_g) of 100, our computed merger rate $\Gamma_{\text{merg}} = 0.010$ Gyr^{-1}, and an average lifetime $\tau \approx 0.3$ Gyr, then we would expect to see 100×0.01 Gyr$^{-1} \times 0.3$ Gyr $= 0.3$ galaxies in this merger stage. This is lower (0.21 galaxies), if we use the numerical value of 0.007 Gyr^{-1}. Given that at least one galaxy is observed in this phase, this implies the minimum boost factor from this method is 3–5. This is a conservative lower limit to the boost fraction, because it implies that there are no close galaxy pairs (within 30 kpc) among any of the other TDE hosts. Indeed, considering that a second TDE has been observed in a close galaxy pair (AT2023clx, Charalampopoulos et al. 2024), then the boost factor doubles to 6–10, consistent with our other method. Again, this is a lower limit to the boost factor, and highlights just how unlikely it is to find TDEs in interacting galaxies if they were not over-represented.

We have clearly shown that there is an over-representation of interacting galaxies hosting TDEs. Given that TDEs are also known to be over-represented in post-starburst galaxies (E + A) (French et al. 2016), it may be tempting to think that the two are connected. The origin of post-starburst galaxies is still somewhat uncertain, with several possible formation channels contributing (Pawlik et al. 2018). However, the most common formation channel, and the most common at this range of stellar masses, is thought to involve a gas-rich merger, which triggers an intense burst of star formation, the growth of the central BH and the growth of a stellar bulge component (Hopkins et al. 2008a; Pawlik et al. 2019). Either the using up of the available gas, or the feedback from the AGN, would then cause a cessation or quenching of the star formation and the galaxy would enter a post-starburst phase (Hopkins et al. 2008b; Li et al. 2023).

In this scenario, mechanisms related to the burst of star formation and the formation of the bulge are expected to enhance the TDE rate, lasting into the quenched star formation phase (French et al. 2018). During the active phases of the BH, TDEs may be difficult to observe. However, once this activity subsides, an increased rate of TDEs should be visible well into the post-starburst phase. The overabundance of TDEs in this post-starburst phase (French et al. 2016; Law-Smith et al. 2017; Graur et al. 2018), together with the recent work from Wevers & French (2024) concluded that their observed increased rate of TDEs in gas-rich post-mergers galaxy very likely indicate an increased rate in mergers, strongly supports this expectation.

However, the appearance of AT 2022wtn suggests that it is in the early stages of the merger rather than in the post-starburst phase. As shown in Section 5.1, the galaxy's SFR does not indicate a recent burst, and the visual appearance with strong tidal tails does not typically occur in the post-starburst phase. Therefore, we may be observing an enhanced TDE rate before the burst/merger/AGN phase. The presence of tidal tails suggests that the galaxy structure is already influenced during the first approach, which would support this observation (Patton et al. 2016). Thus, we may be witnessing the initial enhanced rate of TDEs in interacting galaxies before they enter the AGN/ post-starburst phase, which is consistent with the prediction in Wevers & French (2024). We note that based on mid-IR observations from the *Wide-field Infrared Survey Explorer* satellite, Reynolds et al. (2022) have also suggested a strongly enhanced TDE rate in luminous and ultraluminous infrared galaxies which are often undergoing a major galaxy merger.

8 CONCLUSIONS

8.1 A toy model for AT 2022wtn

AT 2022wtn shows photometric and spectroscopic properties all consistent with a X-ray faint TDE belonging to the TDE-H + He Bowen subclass and it can be explained with the full disruption of a low-mass star (with mass in the range $M_\star \sim 0.1$–0.5 M$_\odot$) by an $M_{\text{BH}} = 10^6$ M$_\odot$ SMBH. On the basis of a number of peculiar behaviours enlightened both from the photometric analysis and the spectroscopic monitoring campaign, we suggest a possible toy model for the AT 2022wtn emission mechanism and for the properties of the emitting region. The full disruption of the low-mass star by the SMBH trigger a prompt circularization phase, leading to an efficient accretion disc formation around the SMBH and the launch of a quasi-spherical fast expanding outflowing reprocessing envelope. These fast outflows could have caused the non-accretion of a substantial fraction of the stellar debris. Indication for the presence of such an outflowing material emerged both in the photometric and spectroscopic analysis, where a fast expanding photosphere and complex line profiles are seen before the detection of a radio emission of transient nature consistent with the AT 2022wtn location. The formation of the new accretion disc produces EUV/X-ray emission, which are not directly observed. However, the detection of Bowen fluorescence lines can be used to infer the EUV/X-ray emission already at early times, together with the presence of a reprocessing envelope and, thus, in the framework of the TDE unified model of Dai et al. (2018), an edge-on view of the system. At later times (after the luminosity maximum plateau) as the photosphere contracts, the He II λ4686 is detected and it is characterized by a line profile narrower than that of the N III λ4640 and of the Hydrogen lines and without showing any particular spectral evolution. This can be explained either with a spatial separation of the regions producing these lines, with the He II λ4686 emitted further out and later on with respect the Bowen and the Hydrogen lines, or by the production of the He II λ4686 in shocks from returning stellar debris streams that are revealed only at late times, when the obscuring photosphere recedes.

8.2 A TDE in an interacting pair of galaxies

Given the peculiar hosting environment, we have carefully investigated the properties of both the interacting galaxies through SED fitting and spectroscopic analysis. Overall, the two galaxies appear of a quite different nature, with the bigger one (SDSS J232323.37 + 104101.7) characterized by a face-on elliptical morphology, a quite passive spectrum (only few lines in emission have been detected: Hα, [N II], and [S II]) and a higher stellar mass. Instead, the AT 2022wtn host galaxy is characterized by the presence of a number of narrow emission lines which indicate a star-forming nature and by a lower SFR with respect to the neighbour galaxy at the peak of the distribution. However, we also find in both galaxies a large drop in the SFR in the last $\sim$Gyr which is similar to what already observed in other TDE hosts. The difference found in the stellar mass of the two galaxies results in a mass ratio of 1:10, which is consistent with a minor merger.

Although based only on two cases (i.e. the only optical TDEs hosted in an interacting pair of galaxies system discovered so far), we have shown that there is indication for an over-representation of merging galaxies hosting TDEs, with an estimated increase of the TDE rate in such systems by a factor of 10. This results is also supported by the recently observed increased rate of TDEs in gas-rich

post-mergers galaxy which in turn very likely indicate an increased rate in mergers (Wevers & French 2024). Specifically for the case of AT 2022wtn, the galaxy's SFR and its visual appearance with strong tidal tails, suggest that it is in the early stages of the merger rather than in the post-starburst phase and that the galaxy structure has been already influenced during the first approach. Thus, we may be indeed witnessing the initial enhanced rate of TDEs before these two galaxies enter in the AGN/post-starburst phase.

This fascinating scenario needs a larger TDE host galaxies sample to be further investigated and the activity of extremely efficient transient survey such as the upcoming Rubin Observatory Legacy Survey of Space and Time (Rubin/LSST), with the predicted increase of the TDE detection rate from 10 to ∼1000 events per year (Bricman & Gomboc 2020), will surely help in resolving the question of the TDE over-representation in merging galaxies in a framework of dedicated statistical studies.

ACKNOWLEDGEMENTS

DATA AVAILABILITY

The photometric data from I:IO/LT, LCOGT and UVOT underlying this article are available in the article itself. The PS1, ATLAS, and ZTF are publicity available. The NTT spectra are publicity available through the PESSTO SSDR4 ESO Phase 4 Data Release (see the ESO archive search and retrieve interface) and on the The Weizmann Interactive Supernova Data Repository (https://www.wiserep.org) The remaining processed spectroscopic data underlying this article are made available as online Supporting Information. All the data set will be also shared on request to the corresponding author.

REFERENCES

Ajith P. et al., 2025, J. Cosmol. Astropart. Phys., 2025, 108
Arcavi I. et al., 2014, ApJ, 793, 38
Baldwin J. A., Phillips M. M., Terlevich R., 1981, PASP, 93, 5
Bellm E. C. et al., 2019, PASP, 131, 018002
Blagorodnova N. et al., 2018, PASP, 130, 035003
Blagorodnova N. et al., 2019, ApJ, 873, 92
Blanchard P. K. et al., 2017, ApJ, 843, 106
Bonnerot C., Lu W., Hopkins P. F., 2021, MNRAS, 504, 4885
Brennan S. J., Fraser M., 2022, A&A, 667, A62
Bricman K., Gomboc A., 2020, ApJ, 890, 73
Bridge C. R. et al., 2010, ApJ, 720, 465
Brown T. M. et al., 2013, PASP, 125, 1031
Buzzoni B. et al., 1984, The Messenger, 38, 9
Cannizzaro G. et al., 2021, MNRAS, 504, 792
Cappellari M., 2017, MNRAS, 466, 798
Cardelli J. A., Clayton G. C., Mathis J. S., 1989, ApJ, 345, 245
Chambers K. C. et al., 2016, preprint (arXiv:1612.05560)
Charalampopoulos P. et al., 2022, A&A, 659, A34
Charalampopoulos P., Pursiainen M., Leloudas G., Arcavi I., Newsome M., Schulze S., Burke J., Nicholl M., 2023, A&A, 673, A95
Charalampopoulos P. et al., 2024, A&A, 689, A350
Christy C. T., Alexander K. D., Laskar T., Berger E., Goodwin A. J., Miller-Jones J. C. A., Chornock R., 2023, Astron. Telegram, 15972, 1
Conselice C. J., Mundy C. J., Ferreira L., Duncan K., 2022, ApJ, 940, 168
Dai L., McKinney J. C., Roth N., Ramirez-Ruiz E., Miller M. C., 2018, ApJ, 859, L20
Esquej P., Saxton R. D., Freyberg M. J., Read A. M., Altieri B., Sanchez-Portal M., Hasinger G., 2007, A&A, 462, L49
Esquej P. et al., 2008, A&A, 489, 543
Evans C. R., Kochanek C. S., 1989, ApJ, 346, L13
Falcón-Barroso J., Sánchez-Blázquez P., Vazdekis A., Ricciardelli E., Cardiel N., Cenarro A. J., Gorgas J., Peletier R. F., 2011, A&A, 532, A95
Ferrarese L., Ford H., 2005, Space Sci. Rev., 116, 523
French K. D., Arcavi I., Zabludoff A., 2016, ApJ, 818, L21
French K. D., Arcavi I., Zabludoff A., 2017, ApJ, 835, 176
French K. D., Yang Y., Zabludoff A. I., Tremonti C. A., 2018, ApJ, 862, 2
French K. D., Wevers T., Law-Smith J., Graur O., Zabludoff A. I., 2020, Space Sci. Rev., 216, 32
Fulton M. et al., 2022, Transient Name Server Classification Report, 2022-3389, 1
Gehrels N. et al., 2004, ApJ, 611, 1005
Gezari S., 2021, ARA&A, 59, 21
Gezari S. et al., 2012, Nature, 485, 217
Gezari S., Cenko S. B., Arcavi I., 2017, ApJ, 851, L47
Gomez S. et al., 2020, MNRAS, 497, 1925
Graham A. W., Scott N., 2013, ApJ, 764, 151
Graham M., Yao Y., Velzen S. V., Gezari S., Hammerstein E., Kulkarni S., 2021, Transient Name Server Classification Report, 2021-2018, 1
Graur O., French K. D., Zahid H. J., Guillochon J., Mandel K. S., Auchettl K., Zabludoff A. I., 2018, ApJ, 853, 39
Guevel D., Hosseinzadeh G., 2017, dguevel/PyZOGY: Initial release. Zenodo
Guillochon J., Ramirez-Ruiz E., 2013, ApJ, 767, 25
Guillochon J., Manukian H., Ramirez-Ruiz E., 2014, ApJ, 783, 23
Guillochon J., Nicholl M., Villar V. A., Mockler B., Narayan G., Mandel K. S., Berger E., Williams P. K. G., 2018, ApJS, 236, 6
Guolo M., Gezari S., Yao Y., van Velzen S., Hammerstein E., Cenko S. B., Tokayer Y. M., 2024, ApJ, 966, 160
Hinkle J. T., Holoien T. W. S., Shappee B. J., Auchettl K., Kochanek C. S., Stanek K. Z., Payne A. V., Thompson T. A., 2020, ApJ, 894, L10
Hinkle J. T. et al., 2022, ApJ, 930, 12
Hinshaw G. et al., 2013, ApJS, 208, 19
Holoien T. W.-S. et al., 2014, MNRAS, 445, 3263
Holoien T. W.-S. et al., 2016a, MNRAS, 455, 2918
Holoien T. W.-S. et al., 2016b, MNRAS, 463, 3813
Hopkins P. F., Hernquist L., Cox T. J., Kereš D., 2008a, ApJS, 175, 356
Hopkins P. F., Cox T. J., Kereš D., Hernquist L., 2008b, ApJS, 175, 390
Hosseinzadeh G., Arcavi I., Howell D. A., Mccully C., Valenti S., 2017, Transient Name Server Classification Report, 2017-241, 1
Huber M. et al., 2015, Astron. Telegram, 7153, 1
Jiang Y.-F., Guillochon J., Loeb A., 2016, ApJ, 830, 125
Jiang N. et al., 2021, ApJS, 252, 32
Jonker P. G., Stone N. C., Generozov A., van Velzen S., Metzger B., 2020, ApJ, 889, 166
Kauffmann G. et al., 2003, MNRAS, 346, 1055
Kennicutt R. C., Jr, 1998, ARA&A, 36, 189
Kewley L. J., Heisler C. A., Dopita M. A., Lumsden S., 2001, ApJS, 132, 37
Kewley L. J., Groves B., Kauffmann G., Heckman T., 2006, MNRAS, 372, 961
Komossa S., 2015, J. High Energy Astrophys., 7, 148
Komossa S., Bade N., 1999, A&A, 343, 775
Kool E. C. et al., 2020, MNRAS, 498, 2167
Law-Smith J., Ramirez-Ruiz E., Ellison S. L., Foley R. J., 2017, ApJ, 850, 22
Leja J., Johnson B. D., Conroy C., van Dokkum P. G., Byler N., 2017, ApJ, 837, 170
Leloudas G. et al., 2019, ApJ, 887, 218
Li W. et al., 2023, MNRAS, 523, 720
Liu X.-L., Dou L.-M., Chen J.-H., Shen R.-F., 2022, ApJ, 925, 67
Lodato G., Rossi E. M., 2011, MNRAS, 410, 359
Lotz J. M., Jonsson P., Cox T. J., Primack J. R., 2010, MNRAS, 404, 575
Lu W., Bonnerot C., 2020, MNRAS, 492, 686
Lu W., Kumar P., Evans N. J., 2016, MNRAS, 458, 575
Magnier E. A. et al., 2020a, ApJS, 251, 3
Magnier E. A. et al., 2020b, ApJS, 251, 5
Makrygianni L. et al., 2023, ApJ, 953, 32
Masterson M. et al., 2024, ApJ, 961, 211
Mattila S. et al., 2018, Science, 361, 482
Merloni A. et al., 2015, MNRAS, 452, 69
Metzger B. D., 2022, ApJ, 937, L12
Metzger B. D., Stone N. C., 2016, MNRAS, 461, 948
Miller J. M. et al., 2015, Nature, 526, 542
Mockler B., Guillochon J., Ramirez-Ruiz E., 2019, ApJ, 872, 151
Mortlock D. J. et al., 2011, Nature, 474, 616
Mundy C. J., Conselice C. J., Duncan K. J., Almaini O., Häußler B., Hartley W. G., 2017, MNRAS, 470, 3507
Neustadt J. M. M. et al., 2020, MNRAS, 494, 2538
Nicholl M., 2018, Res. Notes Am. Astron. Soc., 2, 230
Nicholl M. et al., 2019, MNRAS, 488, 1878
Nicholl M. et al., 2020, MNRAS, 499, 482
Nicholl M. et al., 2023, ApJ, 954, L28
O'Leary J. A., Moster B. P., Krämer E., 2021, MNRAS, 503, 5646
Oke J. B., Sandage A., 1968, ApJ, 154, 21
Oke J. B. et al., 1995, PASP, 107, 375
Onori F. et al., 2019, MNRAS, 489, 1463
Onori F. et al., 2022, MNRAS, 517, 76
Patton D. R., Qamar F. D., Ellison S. L., Bluck A. F. L., Simard L., Mendel J. T., Moreno J., Torrey P., 2016, MNRAS, 461, 2589
Pawlik M. M. et al., 2018, MNRAS, 477, 1708
Pawlik M. M., McAlpine S., Trayford J. W., Wild V., Bower R., Crain R. A., Schaller M., Schaye J., 2019, Nat. Astron., 3, 440
Payne A. V. et al., 2023, ApJ, 951, 134
Perley D. A., 2019, PASP, 131, 084503
Phinney E. S., 1989, in Morris M., ed. IAU Symp. Vol. 136, The Center of the Galaxy, p. 543
Piascik A. S., Steele I. A., Bates S. D., Mottram C. J., Smith R. J., Barnsley R. M., Bolton B., 2014, in Ramsay S. K., McLean I. S., Takami H., eds, Proc. SPIE Conf. Ser. Vol. 9147, Ground-based and Airborne Instrumentation for Astronomy V, p. 91478H
Piran T., Svirski G., Krolik J., Cheng R. M., Shiokawa H., 2015, ApJ, 806, 164
Rees M. J., 1988, Nature, 333, 523
Reusch S. et al., 2022, Phys. Rev. Lett., 128, 221101
Reynolds T. M., Mattila S., Kankare E., Efstathiou A., Kool E., Ryder S., Peña-Moñino L., Pérez-Torres M. A., 2022, A&A, 664, A158

Roth N., Kasen D., 2018, ApJ, 855, 54

Roth N., Kasen D., Guillochon J., Ramirez-Ruiz E., 2016, ApJ, 827, 3

Roth N., Rossi E. M., Krolik J., Piran T., Mockler B., Kasen D., 2020, Space Sci. Rev., 216, 114

Roy R., Mandal S., Sahu D. K., Anupama G. C., Nandi S., Kumar B., 2024, MNRAS, 528, 6176

Ryu T., Krolik J., Piran T., 2020, ApJ, 904, 73

Sánchez-Blázquez P. et al., 2006, MNRAS, 371, 703

Saxton R. D., Read A. M., Esquej P., Komossa S., Dougherty S., Rodriguez-Pascual P., Barrado D., 2012, A&A, 541, A106

Saxton R., Komossa S., Auchettl K., Jonker P. G., 2020, Space Sci. Rev., 216, 85

Schlafly E. F., Finkbeiner D. P., 2011, ApJ, 737, 103

Shingles L. et al., 2021, Transient Name Server AstroNote, 7, 1

Shiokawa H., Krolik J. H., Cheng R. M., Piran T., Noble S. C., 2015, ApJ, 804, 85

Short P. et al., 2020, MNRAS, 498, 4119

Short P. et al., 2023, MNRAS, 525, 1568

Skrutskie M. F. et al., 2006, AJ, 131, 1163

Smartt S. J. et al., 2015, A&A, 579, A40

Smith K. W. et al., 2019, Res. Notes Am. Astron. Soc., 3, 26

Smith K. W. et al., 2020, PASP, 132, 085002

Steele I. A. et al., 2004, in Oschmann J. M., Jr, ed., Proc. SPIE Conf. Ser. Vol. 5489, Ground-based Telescopes, p. 679

Stein R. et al., 2021, Nat. Astron., 5, 510

Steinberg E., Stone N. C., 2024, Nature, 625, 463

Strubbe L. E., Quataert E., 2009, MNRAS, 400, 2070

Tadhunter C., Spence R., Rose M., Mullaney J., Crowther P., 2017, Nat. Astron., 1, 0061

Thomsen L. L., Kwan T. M., Dai L., Wu S. C., Roth N., Ramirez-Ruiz E., 2022, ApJ, 937, L28

Tonry J. L. et al., 2018, PASP, 130, 064505

Toscani M., Rossi E. M., Lodato G., 2020, MNRAS, 498, 507

Trakhtenbrot B. et al., 2019, Nat. Astron., 3, 242

Valenti S. et al., 2014, MNRAS, 438, L101

van Velzen S. et al., 2011, ApJ, 741, 73

van Velzen S., Mendez A. J., Krolik J. H., Gorjian V., 2016, ApJ, 829, 19

van Velzen S. et al., 2019, ApJ, 872, 198

van Velzen S., Holoien T. W. S., Onori F., Hung T., Arcavi I., 2020, Space Sci. Rev., 216, 124

van Velzen S. et al., 2021, ApJ, 908, 4

Waters C. Z. et al., 2020, ApJS, 251, 4

Wevers T., French K. D., 2024, ApJ, 969, L17

Wevers T., Ryu T., 2023, preprint (arXiv:2310.16879)

Wevers T. et al., 2019a, MNRAS, 487, 4136

Wevers T. et al., 2019b, MNRAS, 488, 4816

Wevers T. et al., 2022, A&A, 666, A6

Wong T. H. T., Pfister H., Dai L., 2022, ApJ, 927, L19

Wyrzykowski Ł. et al., 2017, MNRAS, 465, L114

Zabludoff A. et al., 2021, Space Sci. Rev., 217, 54

Zackay B., Ofek E. O., Gal-Yam A., 2016, ApJ, 830, 27

SUPPORTING INFORMATION

Supplementary data are available at *MNRAS* online.

supplementary_spectra.zip

Please note: Oxford University Press is not responsible for the content or functionality of any supporting materials supplied by the authors. Any queries (other than missing material) should be directed to the corresponding author for the article.

APPENDIX A: OPTICAL SPECTROSCOPY

Here, we show the spectral sequence of AT 2022wtn starting ∼5 d from the transient discovery as well as the two spectra of the neighbouring galaxy SDSS J232323.37 + 104101.7, in merging with the AT 2022wtn hosting galaxy (see Fig. A1). In Table A1, we report the spectral fitting results for the N III $\lambda\lambda$4100, 4640; He II λ4686; Hβ; He I λ5875; and Hα emission lines. Data observation and reduction are described in Section 2.

Table A1. Results from the emission-line fit.

Days	Parameters	N III λ4100	N III λ4510	N III λ4640 N	N III λ4640 B	He II λ4686 N	He II λ4686 B
23.66	λ_c [Å]	$\cdots$	$\cdots$	$\cdots$	4641.77 ± 7.27	$\cdots$	$\cdots$
	FWHM [km s^{-1}]	$\cdots$	$\cdots$	$\cdots$	8404 ± 1213	$\cdots$	$\cdots$
	EW [Å]	$\cdots$	$\cdots$	$\cdots$	27.0 ± 5.0	$\cdots$	$\cdots$
49.58	λ_c [Å]	$\cdots$	4503.46 ± 4.34	$\cdots$	4662.36 ± 6.31	$\cdots$	$\cdots$
	FWHM [km s^{-1}]	$\cdots$	2315 ± 716	$\cdots$	10764 ± 1178	$\cdots$	$\cdots$
	EW [Å]	$\cdots$	4.2 ± 1.7	$\cdots$	32.1 ± 4.4	$\cdots$	$\cdots$
53.20	λ_c [Å]	$\cdots$	4518.78 ± 0.86	$\cdots$	4658.51 ± 1.98	$\cdots$	$\cdots$
	FWHM [km s^{-1}]	$\cdots$	1363 ± 137	$\cdots$	8322 ± 329	$\cdots$	$\cdots$
	EW [Å]	$\cdots$	3.1 ± 0.4	$\cdots$	21.4 ± 1.1	$\cdots$	$\cdots$
59.91	λ_c [Å]	4113.63 ± 3.14	$\cdots$	4630.85 ± 1.37	4667.60 ± 5.19	4694.38 ± 1.91	$\cdots$
	FWHM [km s^{-1}]	6795 ± 579	$\cdots$	667 ± 228	6093 ± 642	1431 ± 349	$\cdots$
	EW [Å]	12.4 ± 1.4	$\cdots$	0.78 ± 0.34	10.54 ± 1.55	1.93 ± 0.60	$\cdots$
62.17	λ_c [Å]	$\cdots$	$\cdots$	4635.01 ± 0.54	$\cdots$	4693.88 ± 2.94	$\cdots$
	FWHM [km s^{-1}]	$\cdots$	$\cdots$	1169 ± 88	$\cdots$	4306 ± 510	$\cdots$
	EW [Å]	$\cdots$	$\cdots$	11.2 ± 1.1	$\cdots$	15.9 ± 2.3	$\cdots$
79.78	λ_c [Å]	4076.10 ± 3.76	$\cdots$	4627.39 ± 3.09	$\cdots$	4681.69 ± 3.14	4731.68 ± 38.88
	FWHM [km s^{-1}]	9133 ± 796	$\cdots$	2384 ± 414	$\cdots$	3625 ± 529	23139 ± 6700
	EW [Å]	13.7 ± 1.6	$\cdots$	4.4 ± 1.0	$\cdots$	8.7 ± 1.5	34.0 ± 10.2
105.96	λ_c [Å]	4081.53 ± 3.02	4499.47 ± 6.87	4634.33 ± 1.50	4648.60 ± 2.32	4685.76 ± 0.58	$\cdots$
	FWHM [km s^{-1}]	10427 ± 676	11585 ± 1128	1632 ± 331	7075 ± 442	1238 ± 109	$\cdots$
	EW [Å]	15.0 ± 1.2	12.90 ± 1.56	1.7 ± 0.4	13.9 ± 1.5	2.8 ± 0.3	$\cdots$
232.13	λ_c [Å]	4144.06 ± 14.55	4513.46 ± 9.36	$\cdots$	4619.38 ± 10.36	4683.74 ± 1.42	$\cdots$
	FWHM [km s^{-1}]	11413 ± 3112	6111 ± 1955	$\cdots$	3893 ± 1296	4344 ± 672	$\cdots$
	EW [Å]	10.92 ± 2.22	4.95 ± 1.83	$\cdots$	6.45 ± 2.59	14.28 ± 2.58	$\cdots$
392.84	λ_c [Å]	4051.35 ± 5.77	$\cdots$	$\cdots$	4602.74 ± 20.27	4696.22 ± 7.41	$\cdots$
	FWHM [km s^{-1}]	7200 ± 1126	$\cdots$	$\cdots$	16135 ± 2676	3746 ± 1384	$\cdots$
	EW [Å]	14.08 ± 3.15	$\cdots$	$\cdots$	27.94 ± 6.10	5.50 ± 2.64	$\cdots$

Days	Parameters	H$_\beta$ N	H$_\beta$ B	He I λ5875 N	He I λ5875 B	H$_\alpha$ N	H$_\alpha$ B
23.66	λ_c [Å]	$\cdots$	$\cdots$	5878.34 ± 14.57	$\cdots$	6570.15 ± 1.59	6521.99 ± 22.42
	FWHM [km s^{-1}]	$\cdots$	$\cdots$	6622 ± 1911	$\cdots$	1522 ± 188	13980 ± 3409
	EW [Å]	$\cdots$	$\cdots$	13.4 ± 5.0	$\cdots$	16.1 ± 2.6	38.2 ± 11.6
49.58	λ_c [Å]	4857.25 ± 4.31	$\cdots$	$\cdots$	5852.87 ± 26.13	6571.22 ± 0.91	$\cdots$
	FWHM [km s^{-1}]	4333 ± 693	$\cdots$	$\cdots$	15072 ± 4157	1783 ± 107	$\cdots$
	EW [Å]	12.9 ± 2.6	$\cdots$	$\cdots$	17.9 ± 6.1	25.1 ± 1.9	$\cdots$
53.20	λ_c [Å]	4863.06 ± 0.89	$\cdots$	5876.43 ± 0.93	5843.65 ± 4.31	6566.66 ± 0.25	6566.02 ± 1.25
	FWHM [km s^{-1}]	1847 ± 132	$\cdots$	645 ± 120	7586 ± 566	616 ± 32	3242 ± 142
	EW [Å]	5.2 ± 0.5	$\cdots$	1.4 ± 0.3	13.4 ± 1.3	7.6 ± 0.5	19.8 ± 1.6
59.91	λ_c [Å]	4864.47 ± 1.05	4865.72 ± 3.62	$\cdots$	5881.24 ± 22.72	6565.49 ± 0.11	6557.55 ± 2.63
	FWHM [km s^{-1}]	697 ± 172	6280 ± 663	$\cdots$	13895 ± 3089	476 ± 16	4420 ± 322
	EW [Å]	1.6 ± 0.5	12.8 ± 1.9	$\cdots$	8.8 ± 2.5	13.3 ± 0.5	22.0 ± 2.6
62.17	λ_c [Å]	4893.77 ± 1.64	$\cdots$	$\cdots$	$\cdots$	6569.53 ± 0.53	$\cdots$
	FWHM [km s^{-1}]	1628 ± 242	$\cdots$	$\cdots$	$\cdots$	641 ± 68	$\cdots$
	EW [Å]	6.3 ± 1.2	$\cdots$	$\cdots$	$\cdots$	12.7 ± 1.8	$\cdots$
79.78	λ_c [Å]	4865.20 ± 1.11	4984.70 ± 17.35	5874.52 ± 1.22	5824.52 ± 8.99	6568.80 ± 0.37	6554.31 ± 4.56
	FWHM [km s^{-1}]	2078 ± 188	10130 ± 3005	1154 ± 156	16752 ± 1379	1767 ± 51	8061 ± 660
	EW [Å]	6.3 ± 0.7	9.5 ± 5.1	3.0 ± 0.5	27.5 ± 2.8	35.0 ± 1.3	29.7 ± 3.7
105.96	λ_c [Å]	4861.48 ± 0.09	4835.84 ± 8.70	5877.54 ± 0.30	$\cdots$	6564.35 ± 0.02	6561.75 ± 0.79
	FWHM [km s^{-1}]	430 ± 13	23058 ± 1637	525 ± 41	$\cdots$	309 ± 2	3308 ± 100
	EW [Å]	3.6 ± 0.1	44.8 ± 3.4	2.2 ± 0.2	$\cdots$	20.7 ± 0.2	19.8 ± 1.0
232.13	λ_c [Å]	4863.74 ± 1.42	$\cdots$	$\cdots$	$\cdots$	6568.97 ± 0.44	$\cdots$
	FWHM [km s^{-1}]	1376 ± 213	$\cdots$	$\cdots$	$\cdots$	1781 ± 48	$\cdots$
	EW [Å]	3.1 ± 0.6	$\cdots$	$\cdots$	$\cdots$	47.05 ± 1.67	$\cdots$
392.84	λ_c [Å]	4865.55 ± 2.30	$\cdots$	$\cdots$	$\cdots$	6566.09 ± 10.31	$\cdots$
	FWHM [km s^{-1}]	738 ± 342	$\cdots$	$\cdots$	$\cdots$	991 ± 37	$\cdots$
	EW [Å]	1.52 ± 0.93	$\cdots$	$\cdots$	$\cdots$	35.29 ± 1.55	$\cdots$

Notes. (1) Days from the transient's discovery; (2) fitting parameters, AND (3)−(6) fitting Gaussian component identification (N = narrow and B = broad). With $\cdots$ we indicate the cases in which the component has not been fitted (no component).
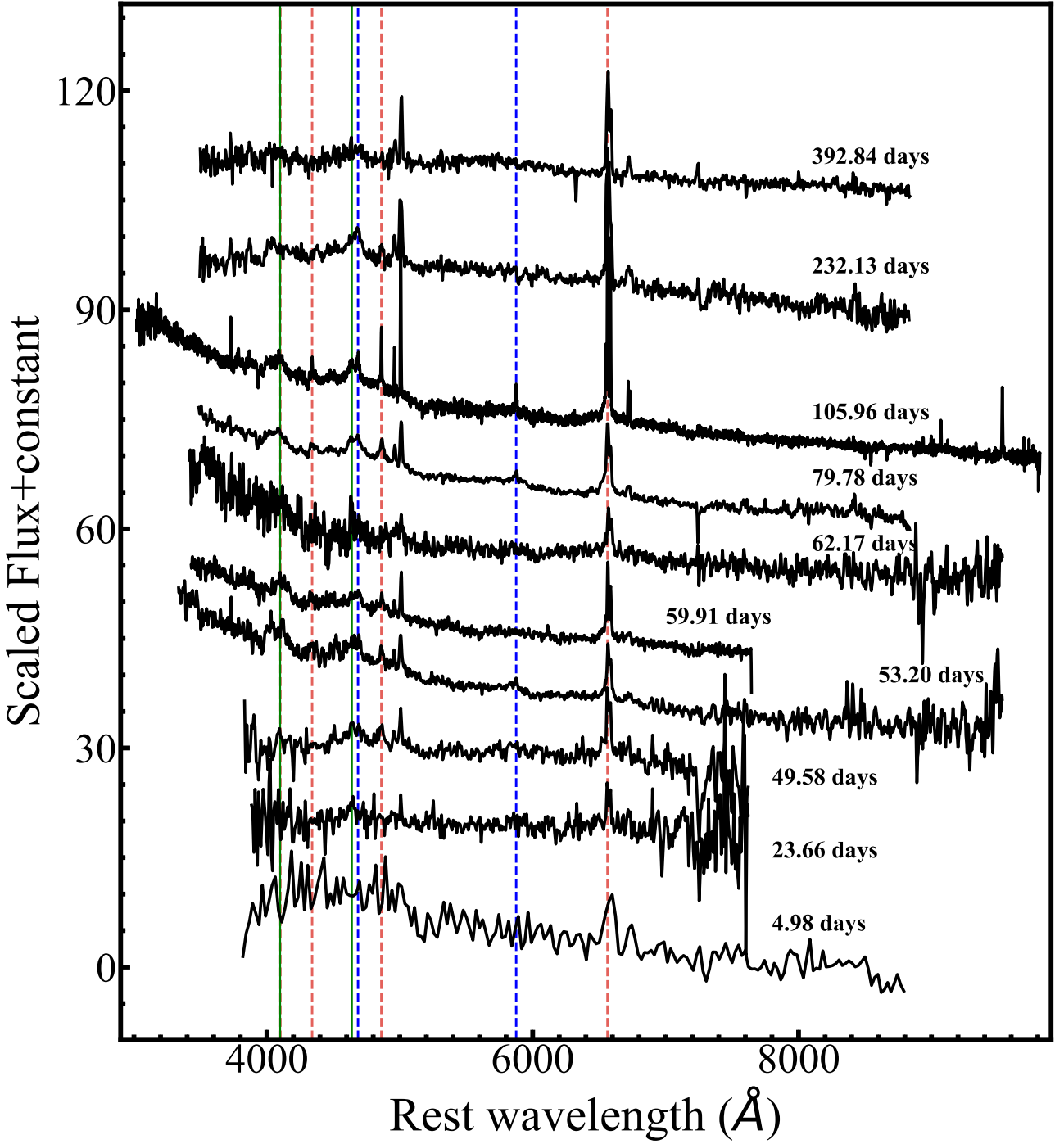
Figure A1. Sequence of AT 2022wtn rest-frame optical spectra corrected for galactic extinction. Days from the transient discovery are shown. The position of the main TDE emission lines are indicated with coloured vertical lines: Hydrogen with red dashed lines, Helium with blue dashed lines, and Bowen lines with green solid lines.

APPENDIX B: UV/OPTICAL PHOTOMETRY

In the following, we report the photometric measurements from the I:O/LT, LCOGT, and *Swift*/UVOT observations (see Tables B1 and B2). In Fig. B1, we show the two-dimensional posteriors obtained from the MOSFIT analysis.

Table B1. I:IO/LT and LCOGT photometric measurements.

MJD (1)	Phase (2)	u' (3)	g' (4)	r' (5)	i' (6)
59 900.84	46.58	17.98 ± 0.06	18.11 ± 0.03	18.29 ± 0.04	18.29 ± 0.02
59 902.01	47.75	17.92 ± 0.10	18.06 ± 0.06	18.24 ± 0.09	18.26 ± 0.04
59 906.09	51.83	⋯	17.99 ± 0.11	18.10 ± 0.14	18.32 ± 0.32
59 906.10	51.84	⋯	18.03 ± 0.10	18.20 ± 0.22	18.25 ± 0.24
59 906.81	52.55	18.01 ± 0.04	18.02 ± 0.03	18.22 ± 0.03	18.32 ± 0.03
59 910.07	55.81	⋯	18.28 ± 0.07	18.35 ± 0.09	18.47 ± 0.20
59 910.08	55.82	⋯	18.26 ± 0.11	18.40 ± 0.08	18.48 ± 0.14
59 913.81	59.55	18.25 ± 0.07	18.26 ± 0.04	18.50 ± 0.03	18.47 ± 0.02
59 914.05	59.79	⋯	18.34 ± 0.13	18.40 ± 0.18	18.58 ± 0.19
59 914.06	59.80	⋯	18.36 ± 0.13	18.45 ± 0.17	18.52 ± 0.20
59 918.08	63.82	⋯	18.35 ± 0.18	18.46 ± 0.21	18.60 ± 0.26
59 918.08	63.82	⋯	18.35 ± 0.18	18.36 ± 0.21	18.42 ± 0.28
59 924.05	69.79	⋯	18.39 ± 0.09	18.60 ± 0.13	18.61 ± 0.18
59 924.06	69.80	⋯	18.41 ± 0.09	18.57 ± 0.12	18.62 ± 0.22
59 927.80	73.54	18.58 ± 0.08	18.59 ± 0.05	18.69 ± 0.04	18.75 ± 0.03
59 928.18	73.92	⋯	18.55 ± 0.11	18.62 ± 0.18	18.89 ± 0.32
59 928.19	73.93	⋯	18.54 ± 0.12	18.65 ± 0.19	18.82 ± 0.30
59 930.43	76.17	⋯	18.71 ± 0.15	18.73 ± 0.18	19.19 ± 0.36
59 933.86	79.60	⋯	18.76 ± 0.10	18.88 ± 0.14	19.02 ± 0.18
59 934.81	80.55	18.84 ± 0.08	18.72 ± 0.05	18.89 ± 0.05	18.82 ± 0.04
59 937.87	83.61	⋯	18.82 ± 0.12	18.87 ± 0.18	18.99 ± 0.23
59 949.05	94.79	⋯	18.88 ± 0.24	18.98 ± 0.26	19.38 ± 0.41
59 953.09	98.83	⋯	18.96 ± 0.16	19.08 ± 0.24	19.07 ± 0.34
59 957.07	102.81	⋯	18.92 ± 0.11	19.06 ± 0.18	19.27 ± 0.27
59 964.08	109.82	⋯	19.08 ± 0.12	19.04 ± 0.27	19.18 ± 0.37
59 971.07	116.81	⋯	19.11 ± 0.26	19.16 ± 0.34	⋯

Notes. (1) MJD date of observations; (2) phase (d) with respect to the discovery date MJD 59 853.28; from (3) to (6) host-subtracted apparent magnitudes and uncertainties for the I:IO/LT and LCOGT u', g', r', and i' filters, reported in AB system. All the magnitudes are uncorrected for foreground extinction. With ⋯ we indicate epochs with no data available (no observations).

Table B2. List of the *Swift* observations executed for the monitoring of AT 2022wtn and the UVOT photometric measurements.

MJD (d) (1)	Phase (d) (2)	XRT exp. time (s) (3)	UVOT exp. time (s) (4)	*UVW*2 (mag) (5)	*UVM*2 (mag) (6)	*UVW*1 (mag) (7)	*U* (mag) (8)	*B* (mag) (9)	*V* (mag) (10)
59 913.76	60.5	1631	1543	16.80 ± 0.05	16.97 ± 0.06	16.94 ± 0.05	⋯	⋯	⋯
59 917.33	64.0	3935	4021	16.88 ± 0.05	16.95 ± 0.06	17.00 ± 0.06	16.92 ± 0.05	17.49 ± 0.04	16.89 ± 0.06
59 927.06	73.8	1529	1530	17.10 ± 0.06	17.18 ± 0.08	17.13 ± 0.07	⋯	⋯	⋯
59 941.00	87.7	1637	1775	17.13 ± 0.07	17.31 ± 0.08	17.23 ± 0.06	⋯	⋯	⋯
59 945.56	92.3	2694	2641	17.27 ± 0.06	17.33 ± 0.08	17.30 ± 0.08	17.27 ± 0.07	17.66 ± 0.06	16.86 ± 0.07
59 949.86	96.6	2858	2806	17.23 ± 0.05	17.21 ± 0.07	17.32 ± 0.08	17.23 ± 0.06	17.65 ± 0.06	16.87 ± 0.07
59 953.23	99.0	1517	1490	17.24 ± 0.06	17.21 ± 0.10	17.47 ± 0.10	17.32 ± 0.09	17.75 ± 0.09	17.03 ± 0.11
59 956.61	102.4	2951	2829	17.22 ± 0.05	17.34 ± 0.09	17.30 ± 0.09	17.21 ± 0.08	17.55 ± 0.07	16.90 ± 0.09
59 965.09	110.8	3257	3203	17.30 ± 0.05	17.50 ± 0.08	17.42 ± 0.08	17.21 ± 0.07	17.74 ± 0.07	16.98 ± 0.08
59 968.08	113.8	1572	1534	17.37 ± 0.07	17.53 ± 0.09	17.32 ± 0.08	⋯	⋯	⋯
59 970.85	116.6	3450	3378	17.35 ± 0.06	17.46 ± 0.08	17.26 ± 0.07	17.32 ± 0.08	17.73 ± 0.07	16.94 ± 0.08
59 974.03	119.8	4212	4135	17.41 ± 0.06	17.46 ± 0.08	17.44 ± 0.08	17.17 ± 0.07	17.64 ± 0.07	16.97 ± 0.09
60 067.22	213.0	3205	3129	17.93 ± 0.08	17.98 ± 0.10	17.87 ± 0.09	17.62 ± 0.09	17.86 ± 0.08	17.11 ± 0.09
60 072.58	218.3	1975	1910	18.05 ± 0.09	18.43 ± 0.20	17.91 ± 0.10	17.68 ± 0.09	17.83 ± 0.08	17.15 ± 0.15
60 077.14	222.9	2999	2925	18.01 ± 0.07	18.09 ± 0.10	17.95 ± 0.10	17.59 ± 0.08	17.88 ± 0.07	16.94 ± 0.08
60 082.04	227.8	2704	2655	18.09 ± 0.07	18.20 ± 0.11	17.86 ± 0.10	17.73 ± 0.09	17.82 ± 0.07	16.94 ± 0.09
60 087.00	232.7	2446	2375	18.20 ± 0.13	18.13 ± 0.17	17.82 ± 0.15	17.55 ± 0.14	17.82 ± 0.12	17.44 ± 0.20
SED FIT	host	-	-	18.41 ± 0.10	18.53 ± 0.10	18.07 ± 0.10	17.70 ± 0.10	17.48 ± 0.10	16.70 ± 0.10

Notes. (1) MJD date of observations; (2) phase (d) with respect to the discovery date MJD 59 853.28; (3) XRT exposure time; (4) UVOT exposure time; from (5) to (10) apparent magnitudes and uncertainties for the UVOT filters *UVW*2, *UVM*2, *UVW*1, *U*, *B*, and *V* reported in Vega system. In the last line, we report the synthetic host UVOT magnitudes (in Vega system) obtained from the AT 2022wtn host galaxy SED fitting. All the magnitudes reported are uncorrected for foreground extinction. With ⋯ we indicate epochs with no data available (no observations). The XRT observations have been obtained in photon counting mode.
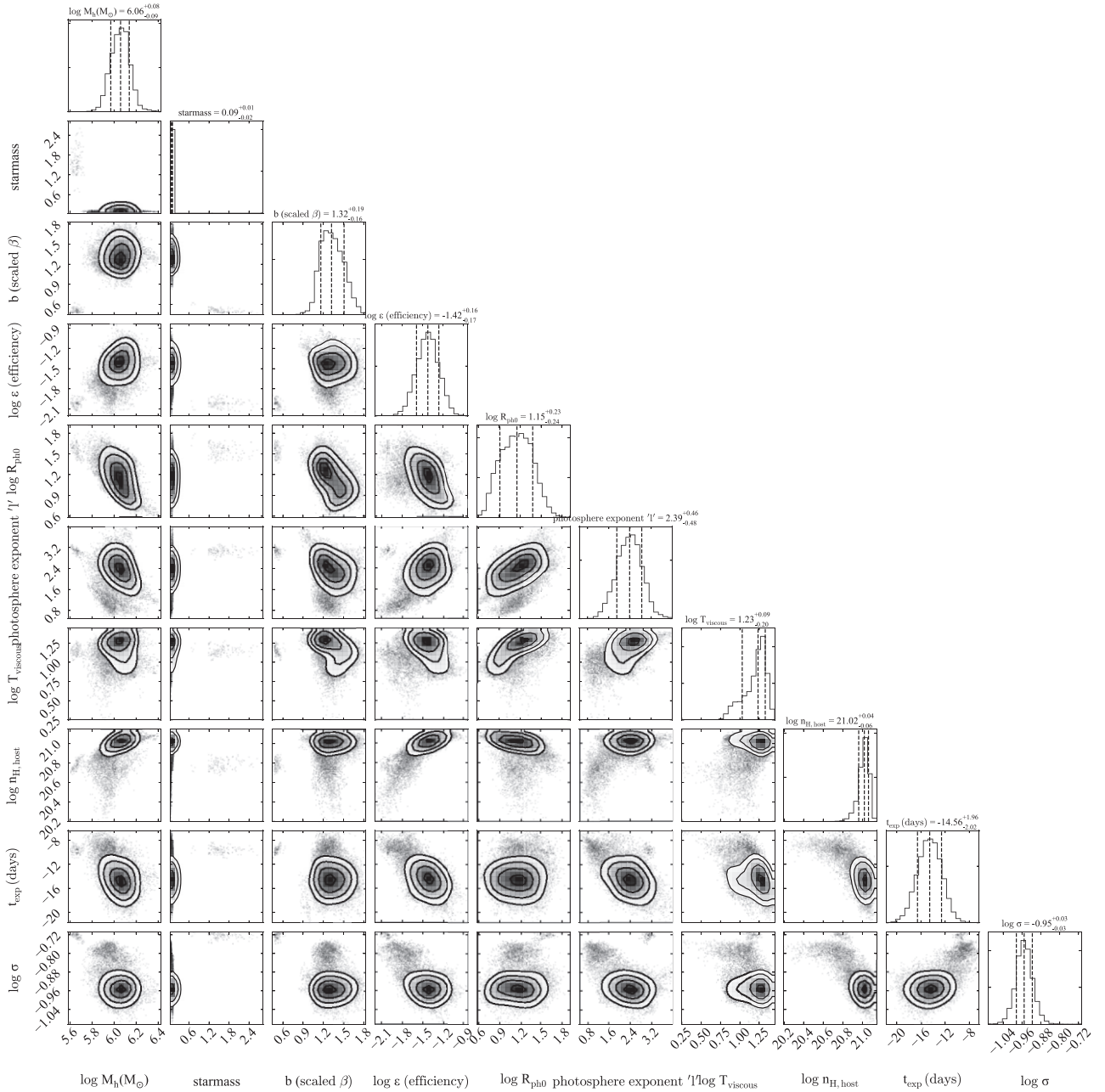
Figure B1. Two-dimensional posteriors resulting from the MOSFIT analysis on the AT 2022wtn photometry.

[1]*INAF – Osservatorio Astronomico d'Abruzzo, via M. Maggini snc, I-64100 Teramo, Italy*

[2]*Astrophysics Research Centre, School of Mathematics and Physics, Queens University Belfast, Belfast BT7 1NN, UK*

[3]*Institute of Gravitational Wave Astronomy & School of Physics and Astronomy, University of Birmingham, Edgbaston, Birmingham B15 2TT, UK*

[4]*Manipal Centre for Natural Sciences, Manipal Academy of Higher Education, Karnataka, Manipal - 576104, India*

[5]*School of Physics and Astronomy, Tel Aviv University, Tel Aviv 69978, Israel*

[6]*European Southern Observatory, Alonso de Córdova 3107, Casilla 19, Santiago, Chile*

[7]*Millennium Institute of Astrophysics MAS, Nuncio Monsenor Sotero Sanz 100, Off 104, Providencia, Santiago, Chile*

[8]*INAF, Osservatorio Astronomico di Roma, Via di Frascati 33, I-00078 Monteporzio, Catone, Italy*

[9]*Center for Astrophysics and Cosmology, University of Nova Gorica, Vipavska 11c, 5270 Ajdovščina, Slovenia*

[10]*Astrophysics Science Division, NASA Goddard Space Flight Center, Greenbelt, MD 20771, USA*

[11]*Joint Space-Science Institute, University of Maryland, College Park, MD 20742, USA*

[12]*Department of Physics and Astronomy, University of Hawaii, 2680 Woodlawn Drive, Honolulu, HI 96822, USA*

[13]*Graduate Institute of Astronomy, National Central University, 300 Jhongda Road, 32001 Jhongli, Taiwan*

[14]*Institute of Cosmology and Gravitation, University of Portsmouth, Portsmouth PO1 3FX, UK*

[15]*Las Cumbres Observatory, 6740 Cortona Drive, Suite 102, Goleta, CA 93117-5575, USA*

[16]*Department of Physics, University of California, Santa Barbara, CA 93106-9530, USA*

[17]*ENEA, NUC Department, Via E. Fermi 45, I-00044 Frascati, Rome, Italy*

[18]*Instituto de Astrofísica e Ciências do Espaço, Faculdade de Ciências, Universidade de Lisboa, Ed. C8, Campo Grande, P-1749-016 Lisbon, Portugal*

[19]*Astronomical Observatory, University of Warsaw, Al. Ujazdowskie 4, PL-00-478 Warszawa, Poland*

[20]*Institut d'Estudis Espacials de Catalunya (IEEC), Edifici RDIT, Campus UPC, E-08860 Castelldefels (Barcelona), Spain*

[21]*Institute of Space Sciences (ICE, CSIC), Campus UAB, Carrer de Can Magrans, s/n, E-08193 Barcelona, Spain*

[22]*Department of Astronomy, University of Maryland, College Park, MD 20742, USA*

[23]*Center for Research and Exploration in Space Science and Technology, NASA/GSFC, Greenbelt, MD 20771, USA*

[24]*Astrophysics Research Institute, Liverpool John Moores University, Liverpool Science Park, 146 Brownlow Hill, Liverpool L3 5RF, UK*

[25]*Cardiff Hub for Astrophysics Research and Technology, School of Physics & Astronomy, Cardiff University, Queens Buildings, The Parade, Cardiff CF24 3AA, UK*

[26]*Department of Physics and Astronomy, University of Turku, FI-20014 Turku, Finland*

[27]*Department of Physics, Royal Holloway – University of London, Egham TW20 0EX, UK*

[28]*Department of Physics, Lancaster University, Lancaster LA1 4YB, UK*

[29]*School of Sciences, European University Cyprus, Diogenes Street, Engomi 1516, Nicosia, Cyprus*

[30]*Instituto de Alta Investigación, Universidad de Tarapacá, Casilla 7D, Arica, Chile*

[31]*Cosmic Dawn Center (DAWN), Niels Bohr Building, Radmandsgade 62-64, DK-2200 Copenhagen, Denmark*

[32]*Niels Bohr Institute, University of Copenhagen, Jagtvej 128, DK-2200 Copenhagen N, Denmark*

[33]*Division of Physics, Mathematics, and Astronomy, California Institute of Technology, Pasadena, CA 91125, USA*

[34]*Key Laboratory of Optical Astronomy, National Astronomical Observatories, Chinese Academy of Sciences, Beijing 100101, P. R. China*

[35]*Space Telescope Science Institute, 3700 San Martin Drive, Baltimore, MD 21218, USA*

[36]*Astrophysics & Space Institute, Schmidt Sciences, New York, NY 10011, USA*

[37]*Miller Institute for Basic Research in Science, 468 Donner Lab, Berkeley, CA 94720, USA*

[38]*Department of Astronomy, University of California, Berkeley, CA 94720, USA*

This paper has been typeset from a TeX/LaTeX file prepared by the author.